Ab initio calculations of the thermoelectric figure of merit, within the relaxation time approximation

L. Chaput, ^{1,2,*} H. Miranda, ³ A. Togo, ⁴ M. Engel, ³ M. Schlipf, ³ M. Marsman, ³ and G. Kresse^{3,5}

¹ Université de Lorraine, LEMTA, CNRS, UMR 7563

² Institut Universitaire de France

³ VASP Software GmbH

⁴ Center for Basic Research on Materials (CBRM),

National Institute for Materials Science (NIMS)

⁵ University of Vienna, Faculty of Physics and Center for Computational Materials Physics

In this paper, we propose a computational framework, based on the VASP and phono3py computer codes, to obtain the thermoelectric figure of merit from the electron-phonon and phonon-phonon interactions using finite displacements in supercells. Several numerical techniques are developed for efficiency.

The method is applied to several thermoelectric materials. We found different behaviors for the lifetimes of the electrons in PbTe, PbSe, and in compounds of the half-Heusler and magnesium silicide family. This is traced back to the different frequencies of the phonons involved in the scattering around the Fermi level. They have a lower frequency in PbTe and PbSe.

The magnitude of the thermoelectric figures of merit we computed compare well with experiments, but the agreement is far from perfect. The role of the defects, not explicitly considered in our calculations, but abundant in thermoelectric materials, is discussed as a possible explanation. It is also shown that the choice of the exchange-correlation functional can strongly impact the results.

I. INTRODUCTION

The study of electronic and thermal transport properties, such as the electronic conductivity (σ) , the thermopower (S), the Peltier coefficient (Π) and the thermal conductivity (κ) dates back to the beginning of the 19th century, often related with names such as Ohm, Seebeck, Peltier and Fourier. About a century later, the electrical and thermal currents obtained from the coexistence of an applied electric field and a temperature gradient was investigated in a thermoelectric generator, whose goal was to produce an electrical current from a temperature difference. It was soon realized that the thermoelectric efficiency of a material in such a generator is maximal when the figure of merit $ZT = \frac{S^2 \sigma}{\kappa} T$ is maximal, even if the theory became fully transparent only with the derivation of Onsager's reciprocity relations and the simple justification of the Kelvin relation 1^{-3} , $\Pi = TS^t$.

Several ab initio calculations of the thermoelectric figure of merit ZT have been performed already^{4–7}, sometimes even including GW correction⁸ or the phonon drag effect⁹. However, such calculations remain challenging because they require the computation of both the phonon-phonon and electron-phonon interactions.

During the last 10 years the computation of the phonon-phonon interactions has become possible^{10,11}, and the computation of the lattice thermal conductivity may now be automatized using workflows. However, often, several methods still need to be combined to compute the electronic transport properties. One may first compute the electronic structure, perform a Wannier transform¹², obtain the electron-phonon interaction^{13,14}, and then solve the transport equation^{15,16}. There are alternatives^{17,18}, however, which encapsulate all those

steps.

To be able to combine several methods has its own merit; it is sometimes the only possible approach to achieve a calculation. However, combining several methods also increases the complexity of the calculations. At each step the calculation may fail for a different reason. Moreover, different convergence parameters need to be considered for the different methods. This makes the calculations difficult to automatize.

In the present paper, we propose an ab initio calculation of the thermoelectric figure of merit based on the finite-difference method for both the calculation of the phonon-phonon and electron-phonon interactions. The computational methods that allow the determination of phonon-phonon and electron-phonon interactions have been discussed in detail in the literature 10,19,20 . In the present work they are integrated in a common workflow to obtain the ZT.

The paper is organized as follows. In the first part of the paper (Sec. II), we briefly review transport theory to establish the notation for future reference. In Sec. III, the workflow of our calculations is explained, and it is applied to several thermoelectric materials in Sec. IV.

II. THERMOELECTRIC TRANSPORT THEORY

A. Thermoelectric transport for electrons

In a semiclassical approximation, the electrical current (\mathbf{J}^e) and heat current (\mathbf{J}^e_O) carried by the electrons can

be written as

$$\mathbf{J}^e = \frac{1}{NV_0} \sum_{\mathbf{k}n} (-e) \mathbf{v}_{\mathbf{k}n} f_{\mathbf{k}n} \tag{1}$$

$$\mathbf{J}_{Q}^{e} = \frac{1}{NV_{0}} \sum_{\mathbf{k}n} (\epsilon_{\mathbf{k}n} - \mu) \mathbf{v}_{\mathbf{k}n} f_{\mathbf{k}n}$$
 (2)

where V_0 is the volume of the primitive cell in the crystal, and N the number of such primitive cells. -e is the charge of the electrons, and μ is the chemical potential. $\epsilon_{\mathbf{k}n}$ and $\mathbf{v}_{\mathbf{k}n}$ are the energy and group velocity of the Bloch states $|\varphi_{\mathbf{k}n}\rangle$ with wave vector \mathbf{k} and band index n. $f_{\mathbf{k}n}$ is the occupation of the state $|\varphi_{\mathbf{k}n}\rangle$ when an electrical field and a temperature gradient are applied to the crystal.

In our approach, $|\varphi_{\mathbf{k}n}\rangle$ are taken to be the Kohn-Sham states obtained from density functional theory. The chemical potential μ is computed from the number of electrons n_0 in the primitive cell,

$$n_0 = \int_{-\infty}^{+\infty} d\epsilon \, \rho(\epsilon) f_{\mathbf{k}n}^0(\epsilon, T, \mu), \tag{3}$$

where $f^{0}(\epsilon, T, \mu)$ is the Fermi-Dirac occupation function,

$$f^{0}(\epsilon, T, \mu) = \frac{1}{\exp\frac{\epsilon - \mu}{k_{B}T} + 1},\tag{4}$$

with k_B the Boltzmann constant and T the temperature. $\rho(\epsilon)$ is the density of states,

$$\rho(\epsilon) = \frac{1}{N} \sum_{\mathbf{k}n} \delta(\epsilon - \epsilon_{\mathbf{k}n}). \tag{5}$$

In the following sections, when doped compounds will be considered, Eq. 3 will be used to compute the chemical potential in the rigid band approximation. It means that this equation will be solved for μ taking for n_0 the number of electrons in the doped compound, but for $\rho(\epsilon)$ the density of states of the perfect crystal.

To compute the currents in Eqs. 1 and 2, the velocity and the occupation function must be computed. The computation of the velocity is explained in appendix D when the Kohn Sham equations are solved using the projector-augmented-wave (PAW) method^{21–26}. The occupation function $f_{\mathbf{k}n}(\mathbf{r})$ is obtained from a Boltzmann equation,

$$\frac{\partial f_{\mathbf{k}n}}{\partial t} + \mathbf{v}_{\mathbf{k}n} \cdot \frac{\partial f_{\mathbf{k}n}}{\partial \mathbf{r}} + \frac{-e}{\hbar} \mathbf{E} \cdot \frac{\partial f_{\mathbf{k}n}}{\partial \mathbf{k}} = \frac{\partial f_{\mathbf{k}n}}{\partial t} \Big|_{col}.$$
 (6)

The right-hand side of the above equation is a collision integral and gives the change, per unit time, of the number of electrons in state $|\varphi_{\mathbf{k}n}\rangle$ due to collisions. In the present study, we consider collisions caused by electron-phonon interactions. Therefore if we denote by $g(\mathbf{k}n, \mathbf{k}'n', \mathbf{q}j)$ the electron-phonon coupling strength of the electron-phonon Hamiltonian

$$H_{ep} = \sum_{\mathbf{k}n} \sum_{\mathbf{k}'n'} \sum_{\mathbf{q}j} g(\mathbf{k}n, \mathbf{k}'n', \mathbf{q}j) (a_{\mathbf{q}j} + a_{-\mathbf{q}j}^{\dagger}) c_{\mathbf{k}n}^{\dagger} c_{\mathbf{k}'n'}, \tag{7}$$

where $a_{\mathbf{q}j}$ and $a_{\mathbf{q}j}^{\dagger}$ are the phonon annihilation and creation operators in mode $\mathbf{q}j$, and $c_{\mathbf{k}n}$ and $c_{\mathbf{k}n}^{\dagger}$ the electron annihilation and creation operators in Bloch state $\mathbf{k}n$, Fermi's golden rule gives

$$\frac{\partial f_{\mathbf{k}n}}{\partial t}\Big|_{col} = \frac{2\pi}{\hbar} \sum_{\mathbf{k}'n'} \sum_{\mathbf{q}j} |g(\mathbf{k}n, \mathbf{k}'n', \mathbf{q}j)|^2 \Big[\delta(\epsilon_{\mathbf{k}n} - \epsilon_{\mathbf{k}'n'} - \hbar\omega_{\mathbf{q}j}) \Big((1 - f_{\mathbf{k}n}) f_{\mathbf{k}'n'} n_{\mathbf{q}j} - f_{\mathbf{k}n} (1 - f_{\mathbf{k}'n'}) (1 + n_{\mathbf{q}j}) \Big) \\
+ \delta(\epsilon_{\mathbf{k}n} - \epsilon_{\mathbf{k}'n'} + \hbar\omega_{-\mathbf{q}j}) \Big((1 - f_{\mathbf{k}n}) f_{\mathbf{k}'n'} (1 + n_{-\mathbf{q}j}) - f_{\mathbf{k}n} (1 - f_{\mathbf{k}'n'}) n_{-\mathbf{q}j} \Big) \Big]. \tag{8}$$

In the above equation the summations are performed over the first Brillouin zone, and the momentum conservation, $\mathbf{k} = \mathbf{k}' + \mathbf{q} \mod \mathbf{G}$, is included in the definition of $g(\mathbf{k}n, \mathbf{k}'n', \mathbf{q}j)$. $n_{\mathbf{q}j}$ is the occupation function of phonons with mode $\mathbf{q}j$ and energy $\hbar\omega_{\mathbf{q}j}$, which at equilibrium equals the Bose-Einstein occupation function,

$$n^{0}(\omega, T) = \frac{1}{\exp\frac{\hbar\omega}{k_{B}T} - 1}.$$
(9)

If the applied fields **E** and ∇T are small, the Boltzmann equation in Eq. 6 can be linearized. Writing $f_{\mathbf{k}n} = f_{\mathbf{k}n}^0 + \delta f_{\mathbf{k}n}$ and $n_{\mathbf{q}j} = n_{\mathbf{q}j}^0 + \delta n_{\mathbf{q}j}$, with $f_{\mathbf{k}n}^0 = f^0(\epsilon_{\mathbf{k}n}, T, \mu)$ and $n_{\mathbf{q}j}^0 = n^0(\omega_{\mathbf{q}j}, T)$, and assuming $\delta f_{\mathbf{k}n}$ and $\delta n_{\mathbf{q}j}$ to be of order 1 in the applied fields, from chain rules over **r** and **k**, in steady state, we obtain²⁷

$$\left((\epsilon_{\mathbf{k}n} - \mu) \frac{\nabla T}{T} + e \mathcal{E} \right) \cdot \mathbf{v}_{\mathbf{k}n} \left(-\frac{\partial f_{\mathbf{k}n}^0}{\partial \epsilon_{\mathbf{k}n}} \right) = \frac{\partial f_{\mathbf{k}n}}{\partial t} \Big|_{lin}, \tag{10}$$

with $\mathcal{E} = \mathbf{E} + \nabla \mu / e$ and

$$\frac{\partial f_{\mathbf{k}n}}{\partial t}\Big|_{lin} = -\frac{2\pi}{\hbar} \sum_{\mathbf{k}'n'} \sum_{\mathbf{q}j} |g(\mathbf{k}n, \mathbf{k}'n', \mathbf{q}j)|^2 \Big((1 + n_{\mathbf{q}j}^0 - f_{\mathbf{k}'n'}^0) \delta(\epsilon_{\mathbf{k}n} - \epsilon_{\mathbf{k}'n'} - \hbar\omega_{\mathbf{q}j}) + (f_{\mathbf{k}'n'}^0 + n_{-\mathbf{q}j}^0) \delta(\epsilon_{\mathbf{k}n} - \epsilon_{\mathbf{k}'n'} + \hbar\omega_{-\mathbf{q}j}) \Big) \delta f_{\mathbf{k}n} + \frac{2\pi}{\hbar} \sum_{\mathbf{k}'n'} \sum_{\mathbf{q}j} |g(\mathbf{k}n, \mathbf{k}'n', \mathbf{q}j)|^2 \Big((n_{\mathbf{q}j}^0 + f_{\mathbf{k}n}^0) \delta(\epsilon_{\mathbf{k}n} - \epsilon_{\mathbf{k}'n'} - \hbar\omega_{\mathbf{q}j}) + (1 + n_{-\mathbf{q}j}^0 - f_{\mathbf{k}n}^0) \delta(\epsilon_{\mathbf{k}n} - \epsilon_{\mathbf{k}'n'} + \hbar\omega_{-\mathbf{q}j}) \Big) \delta f_{\mathbf{k}'n'} + \frac{2\pi}{\hbar} \sum_{\mathbf{k}'n'} \sum_{\mathbf{q}j} |g(\mathbf{k}n, \mathbf{k}'n', \mathbf{q}j)|^2 (f_{\mathbf{k}'n'} - f_{\mathbf{k}n}) \Big(\delta(\epsilon_{\mathbf{k}n} - \epsilon_{\mathbf{k}'n'} - \hbar\omega_{\mathbf{q}j}) \delta n_{\mathbf{q}j} + \delta(\epsilon_{\mathbf{k}n} - \epsilon_{\mathbf{k}'n'} + \hbar\omega_{-\mathbf{q}j}) \delta n_{-\mathbf{q}j} \Big). \tag{11}$$

To solve the Boltzmann equation, the phonon system is assumed to remain at equilibrium, $\delta n_{\mathbf{q}j} = 0$, then the third line of the above equation vanishes. If one wishes to go beyond this approximation, the phonon Boltzmann equation need to be solved self-consistently together with the one for electrons. This is, for example, needed to describe the phonon drag effect.

Even assuming the phonon system to be in equilibrium, the Boltzmann equation is still an integral equation, since the second line of the previous equation involves a sum over the Brillouin zone. It can be solved exactly, but in the present paper, we will use simpler approximations based on relaxation times.

The most common approximation is to simply neglect the second line of Eq. 11. It amounts to assume $\delta f_{\mathbf{k}'n'} = 0$, or in other words, that the change in the number of electrons in any other state than the state under consideration, $\mathbf{k}n$, is not changed by the collisions. This is the usual relaxation-time approximation, now called self-energy relaxation-time approximation (SERTA) to emphasize that the collision integral can be written as

$$\left. \frac{\partial f_{\mathbf{k}n}}{\partial t} \right|_{\text{SERTA}} = -\frac{\delta f_{\mathbf{k}n}}{\tau_{\mathbf{k}n}^{\text{SERTA}}}$$
 (12)

where $1/\tau_{\mathbf{k}n}^{\text{SERTA}}$ is twice the imaginary part of the Fan-Migdal self-energy,

$$\frac{1}{\tau_{\mathbf{k}n}^{\text{SERTA}}} = \frac{2\pi}{\hbar} \sum_{\mathbf{k'}n'} \sum_{\mathbf{q}j} |g(\mathbf{k}n, \mathbf{k'}n', \mathbf{q}j)|^2 w_{\mathbf{k}n, \mathbf{k'}n'}$$
(13)

$$\times \left((1 + n_{\mathbf{q}j}^{0} - f_{\mathbf{k}'n'}^{0}) \delta(\epsilon_{\mathbf{k}n} - \epsilon_{\mathbf{k}'n'} - \hbar\omega_{\mathbf{q}j}) + (f_{\mathbf{k}'n'}^{0} + n_{-\mathbf{q}j}^{0}) \delta(\epsilon_{\mathbf{k}n} - \epsilon_{\mathbf{k}'n'} + \hbar\omega_{-\mathbf{q}j}) \right). \tag{14}$$

In the above equation, the weighting factor $w_{\mathbf{k}n,\mathbf{k}'n'}$ is 1. In other words, the relaxation time is equal to the lifetime. However different approximations can be obtained considering different values for $w_{\mathbf{k}n,\mathbf{k}'n'}$. Two other usual approximations^{17,28,29}, the momentum relaxation-time approximation (MRTA) and the energy relaxation-time approximation (ERTA) are derived in Appendix B. In those cases, we have

$$w_{\mathbf{k}n,\mathbf{k}'n'} = 1 - \frac{\mathbf{v}_{\mathbf{k}n} \cdot \mathbf{v}_{\mathbf{k}'n'}}{|\mathbf{v}_{\mathbf{k}n}||\mathbf{v}_{\mathbf{k}'n'}|}$$
 for MRTA, (15)

$$w_{\mathbf{k}n,\mathbf{k}'n'} = 1 - \frac{|\epsilon_{\mathbf{k}'n'} - \mu|}{|\epsilon_{\mathbf{k}n} - \mu|} \frac{\mathbf{v}_{\mathbf{k}n} \cdot \mathbf{v}_{\mathbf{k}'n'}}{|\mathbf{v}_{\mathbf{k}n}||\mathbf{v}_{\mathbf{k}'n'}|}$$
for ERTA. (16)

The MRTA approximation is derived assuming there is no temperature gradient. Its weighting factor makes large-angle scatterings important for the resistivity. The ERTA is obtained considering a temperature gradient alone. It is often assumed^{29–31} that for heat conduction all scattering processes are equally effective. Therefore, this factor is sometimes neglected, and the SERTA is used instead. This is the assumption which will be used in this paper. The differences between ERTA, SERTA and MRTA will be considered in more detail in a future work, as it requires a careful treatment for numerical stability^{31,32}. For a coupled electric field and a thermal gradient applied on the system, those approximations become weaker. Finally, an even simpler approximation is the constant relaxation time approximation (CRTA), in which the relaxation time $\tau_{\mathbf{k}n}$ is assumed to be independent of the electronic state, i.e. $\tau_{\mathbf{k}n} = \tau$. A typical value is $\tau = 10^{-14}$ s, which will be adopted whenever the CRTA is applied in this work.

Using one of the above mentioned relaxation-time approximations to solve Eq. 10, we obtain

$$\delta f_{\mathbf{k}n} = -\tau_{\mathbf{k}n} \left((\epsilon_{\mathbf{k}n} - \mu) \frac{\nabla T}{T} + e \mathcal{E} \right) \cdot \mathbf{v}_{\mathbf{k}n} \left(-\frac{\partial f_{\mathbf{k}n}^0}{\partial \epsilon_{\mathbf{k}n}} \right)$$
(17)

and therefore Eqs. 1 and 2 give

$$\mathbf{J}^e = \mathcal{L}_{11} \mathcal{E} + \mathcal{L}_{12} \frac{-\nabla T}{T},\tag{18}$$

$$\mathbf{J}_{Q}^{e} = \mathcal{L}_{21}\mathcal{E} + \mathcal{L}_{22}\frac{-\nabla T}{T},\tag{19}$$

with

$$\mathcal{L}_{11} = \frac{1}{NV_0} \sum_{\mathbf{k}_n} (e^2) \tau_{\mathbf{k}n} \mathbf{v}_{\mathbf{k}n} \otimes \mathbf{v}_{\mathbf{k}n} \left(-\frac{\partial f_{\mathbf{k}n}^0}{\partial \epsilon_{\mathbf{k}n}} \right), \tag{20}$$

$$\mathcal{L}_{12} = \mathcal{L}_{21} = \frac{1}{NV_0} \sum_{\mathbf{k}n} (-e)(\epsilon_{\mathbf{k}n} - \mu) \tau_{\mathbf{k}n} \mathbf{v}_{\mathbf{k}n} \otimes \mathbf{v}_{\mathbf{k}n} \left(-\frac{\partial f_{\mathbf{k}n}^0}{\partial \epsilon_{\mathbf{k}n}} \right), \tag{21}$$

$$\mathcal{L}_{22} = \frac{1}{NV_0} \sum_{\mathbf{k}n} (\epsilon_{\mathbf{k}n} - \mu)^2 \tau_{\mathbf{k}n} \mathbf{v}_{\mathbf{k}n} \otimes \mathbf{v}_{\mathbf{k}n} \Big(-\frac{\partial f_{\mathbf{k}n}^0}{\partial \epsilon_{\mathbf{k}n}} \Big).$$
 (22)

The Onsager coefficients \mathcal{L}_{ij} can be written as

$$\mathcal{L}_{ij} = \int d\epsilon \, \sigma(\epsilon) \left(\frac{\epsilon - \mu}{-e}\right)^{i+j-2} \left(-\frac{\partial f^0}{\partial \epsilon}\right)$$
 (23)

with

$$\sigma(\epsilon) = \frac{e^2}{NV_0} \sum_{\mathbf{k}n} \tau_{\mathbf{k}n} \mathbf{v}_{\mathbf{k}n} \otimes \mathbf{v}_{\mathbf{k}n} \delta(\epsilon_{\mathbf{k}n} - \epsilon). \tag{24}$$

Notice that, as for the density of states, a factor 2 needs to be included for spin, if not included in the summation over bands. The transport function $\sigma(\epsilon)$ represents the conductivity of electrons with energy ϵ , and therefore its unit is $(\Omega \cdot m)^{-1}$. One could directly compute the Onsager coefficients from an accumulation over the Brillouin zone using Eqs. 20, 21 and 22. However, it is numerically advantageous to first compute the transport function $\sigma(\epsilon)$ and then the Onsager coefficient \mathcal{L}_{ij} through an integration over energy. Indeed, $\sigma(\epsilon)$ can be computed using the tetrahedron method, which is a (linear) interpolation method and allows to use a coarser sampling of the Brillouin zone. To perform the integrals over energy, we use a Gauss-Legendre quadrature which is explained in Appendix C. The electronic conductivity (σ) , the thermopower (S) and the electronic part of the thermal conductivity (κ_e) are finally expressed as

$$\sigma = \mathcal{L}_{11},\tag{25}$$

$$S = \frac{1}{T} \mathcal{L}_{11}^{-1} \mathcal{L}_{12},\tag{26}$$

$$\kappa_e = \frac{1}{T} (\mathcal{L}_{22} - \mathcal{L}_{21} \mathcal{L}_{11}^{-1} \mathcal{L}_{12}). \tag{27}$$

B. Thermoelectric transport for phonons

In this section, we consider the lattice thermal conductivity κ_L . The details of the calculations are given in Ref. 10. In particular, in this work, it is assumed that the phonons are only scattered by other phonons, and therefore the effect of the electron-phonon interactions on phonons is neglected. The lifetime of the phonons is obtained from Fermi's golden rule on a Hamiltonian containing anharmonicity up to third order in the atomic displacements of the atoms around their equilibrium positions,

$$H_{pp} = \sum_{\mathbf{q}_1 j_1} \sum_{\mathbf{q}_2 j_2} \sum_{\mathbf{q}_3 j_3} \Phi(\mathbf{q}_1 j_1, \mathbf{q}_2 j_2, \mathbf{q}_3 j_3) (a_{\mathbf{q}_1 j_1} + a_{-\mathbf{q}_1 j_1}^{\dagger}) (a_{\mathbf{q}_2 j_2} + a_{-\mathbf{q}_2 j_2}^{\dagger}) (a_{\mathbf{q}_3 j_3} + a_{-\mathbf{q}_3 j_3}^{\dagger}). \tag{28}$$

The strength Φ of this interaction is given by the Fourier transform of the third derivative of the energy with respect to atomic positions, projected onto the eigenvectors of the phonons participating in the interaction. As for the electron-phonon interaction, it includes the momentum conservation. The lifetime is then given by

$$\frac{1}{\tau_{\mathbf{q}j}} = \frac{36\pi}{\hbar^2} \sum_{\mathbf{q}_2 j_2} \sum_{\mathbf{q}_3 j_3} |\Phi(-\mathbf{q}j, \mathbf{q}_2 j_2, \mathbf{q}_3 j_3)|^2 \times \left[(n_{\mathbf{q}_2 j_2}^0 + n_{\mathbf{q}_3 j_3}^0 + 1) \delta(\omega_{\mathbf{q}j} - \omega_{\mathbf{q}_2 j_2} - \omega_{\mathbf{q}_3 j_3}) + 2(n_{\mathbf{q}_2 j_2}^0 - n_{\mathbf{q}_3 j_3}^0) \delta(\omega_{\mathbf{q}j} - \omega_{\mathbf{q}_2 j_2} + \omega_{\mathbf{q}_3 j_3}) \right]. \tag{29}$$

In the relaxation-time approximation, the lattice thermal conductivity is computed from

$$\kappa_L = \frac{1}{NV_0} \sum_{\mathbf{q}j} C_{\mathbf{q}j} \tau_{\mathbf{q}j} \mathbf{v}_{\mathbf{q}j} \otimes \mathbf{v}_{\mathbf{q}j}, \tag{30}$$

with the mode heat capacity $C_{\mathbf{q}j} = \frac{\partial}{\partial T} \hbar \omega_{\mathbf{q}j} n_{\mathbf{q}j}^0$ and the group velocity $\mathbf{v}_{\mathbf{q}j} = \frac{\partial \omega_{\mathbf{q}j}}{\partial \mathbf{q}}$.

III. COMPUTATIONAL STRATEGIES

A. Integration over energy

To compute the Onsager coefficients from Eq. 23 the electronic relaxation times and the electron group velocities are needed. A naive implementation would require the computation of those relaxation times for all the Kohn-Sham states. However, we can limit the computation of relaxation times to states whose energies lie within the energy range spanned by a Gauss-Legendre integration grid.

Indeed, in Appendix C, the integral over energy Eq. 23 is replaced by an integration over x using $\epsilon = \mu +$ $k_BT \ln \frac{1+x}{1-x}$, with x in the range (-1,1). The x axis is discretized using $\{x_k\}_{k=1...N}$, the N roots of the Legendre polynomial $P_N(x)$. N is a convergence parameter. It is the number of points in the interval (1,-1)and therefore controls the size of the integration step. However, it also controls the size of the energy window around the chemical potential over which the integration is performed. Indeed, in Fig. 1 (a), the function $\ln(1+x)/(1-x)$, which measures the range of the energy window around the chemical potential, in units of k_BT , is plotted with respect to the roots x_k for several values of N. The roots change with N, and in particular, x_N , the largest root, approaches 1 as N increases. In fact, we have the estimate^{33,34} $\cos \pi \frac{1}{N+1/2} < x_N < \cos \pi \frac{1/2}{N+1/2}$. This means that $\ln[(1+x_N)/(1-x_N)]$ may become large for large N (see Fig. 1 (b)), and therefore the energy range over which the relaxation time needs to be computed may become large as well. Fortunately, to perform the integrals in Eq. 23, it has been found from the examples we considered that moderate values of N, around N = 501, are sufficient. The energy range around the chemical potential may be restricted because of the fast decay of the derivative of the Fermi-Dirac function as the energy increases, but it can also be restricted because the integration weights w_k decrease as $x_k \to \pm 1$, and as N increases (see Fig. 1 (c)). This strategy speeds up the calculation while allowing control over the accuracy and computational cost using a single parameter, the number of integration points N of the Gauss-Legendre grid.

B. Calculation steps

The relaxation times given by Eqs. 14, 15 and 16 are computed from the electron-phonon interaction

 $g(\mathbf{k}n, \mathbf{k}'n', \mathbf{q}j)$. Details about the theory are given in Ref. 19 for the PAW method. In a few words, to compute $g(\mathbf{k}n, \mathbf{k}'n', \mathbf{q}j)$, the derivatives of the local and non-local potentials are computed by applying finite displacements to atoms in supercells. The derivatives are obtained from the changes in the potentials using finite differences.

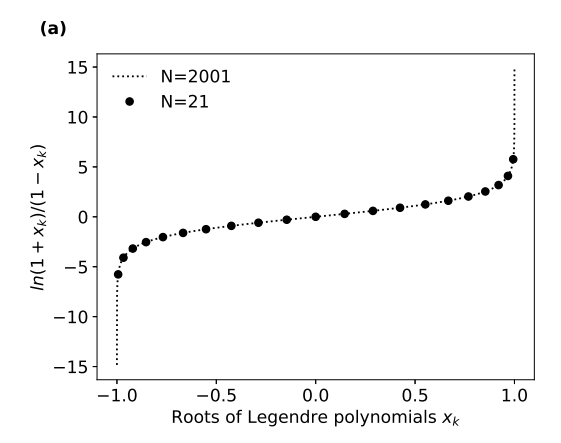
If we go more into the details of such calculation, a series of computations are necessary to obtain $g(\mathbf{k}n, \mathbf{k}'n', \mathbf{q}j)$ and the transport properties. They are all organized using a command line tool of the phelel code³⁵, allowing to prepare the inputs of every VASP calculation, using outputs from previous ones. The general setting of the calculations, such as cut-off energy, Brillouin zone sampling, etc, are obtained from a separate file, defined prior to the start of the calculations, and read by phelel when the inputs of the VASP calculations are being prepared. This approach is convenient because the series of calculations needed to obtain the electronphonon interactions and the transport properties can be seen as operated by phelel. The series of calculations can then be summarized as a small number of simple phelel commands

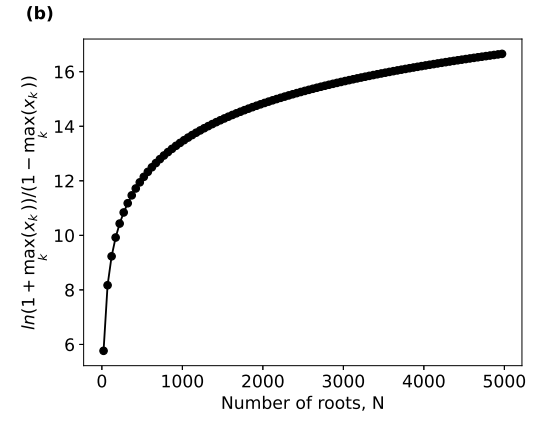
The different steps, detailed below for the computations performed in this work, can be categorized as preparatory, and steps related to the computation of the derivatives of the potentials, and transport steps. They are respectively indexed as (a-b), (c-e), and (f) in the following.

The preparatory steps may be optional. In this study, (a) the crystal structure is relaxed. Then, (b) using the relaxed crystal structure, dielectric constants and Born effective charges are computed. This step is required because the compounds we consider in our study have an ionic contribution.

In step (c-e), the potential derivatives are computed. The method is summarized in Fig. 2. At step (c) the supercells with displacements are generated using the phelel code, considering symmetry. Then, (d) a series of VASP calculations is performed to obtain changes in the potentials. In step (e) the potential derivatives are computed from the results of the VASP calculations using the phelel code, and are stored in a file, phelel_params.hdf5. For that step, phelel uses the finufft³⁶ library to perform a nonuniform fast Fourier transform from the grid points in the supercells to the grid points in a primitive cell on which the wavefunctions will later be known.

In a final step, (f), VASP reads the phelel_params.hdf5 file to compute $g(\mathbf{k}n, \mathbf{k}'n', \mathbf{q}j)$ and the transport properties. This step is detailed in the next section.





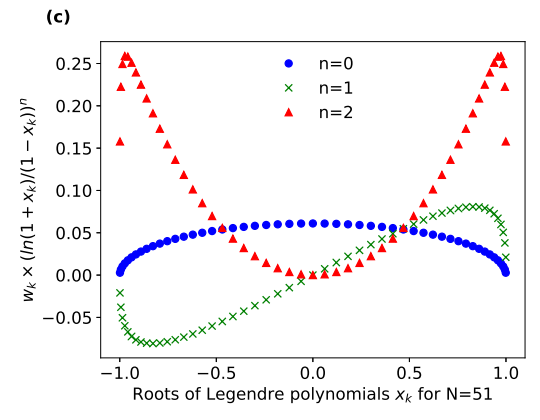


FIG. 1. Gauss-Legendre integration grids: (a) $\ln[(x+1)/(x-1)]$ the range of the energy window in units of k_BT around the chemical potential μ , for N=21 and N=2001, (b) $\ln[(x_N+1)/(x_N-1)]$, with x_N the largest root, as a function of the number of roots N, (c) function in the integrand of Eq. C1, $\left(\ln[(1+x_k)(1-x_k)]\right)^n w_k$, as a function of the x_k , for n=0,1,2.

C. Electron-phonon matrix elements

To obtain $g(\mathbf{k}n, \mathbf{k}'n', \mathbf{q}j)$, the integration in $\langle \varphi_{\mathbf{k}n} | \partial \tilde{h} / \partial \mathbf{R} | \varphi_{\mathbf{k}'n'} \rangle$ should be performed over a supercell, with \mathbf{k} , \mathbf{k}' and \mathbf{q} within the Brillouin zone of a primitive cell¹⁹. Indeed, the potential derivatives

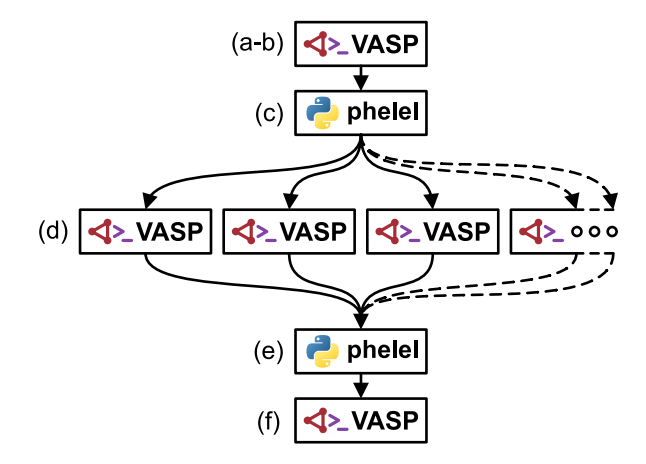


FIG. 2. Flow chart for the calculation of electronic transport properties using VASP and phelel. (a) Preparatory steps are performed using the VASP code. (c) Supercell structures are generated with phelel. (d) Each displaced structure is then run as an individual VASP calculation. (e) The results are gathered by phelel to compute the potential derivatives and transferred to the primitive cell. (f) The final VASP calculation in the primitive cell then calculates the electron-phonon interactions and transport properties.

contained in phelel_params.hdf5 are known within the supercell. Therefore, to perform the integral, one should expand the orbitals from the primitive cell, known from the final VASP step in Fig. 2, to the supercell using Bloch's theorem. However, in practice, we use the opposite strategy to integrate over a primitive cell. Instead of expanding the Bloch functions from the primitive cell to the supercell, the potential derivatives are downfolded from the supercell to the primitive cell. For example, Eq. A21 in Ref. 20 can be written as an integral over V_0

$$\int_{V_0} d^3 \mathbf{r} \, \tilde{u}_{\mathbf{k}n}^*(\mathbf{r}) \tilde{v}_{\kappa}(\mathbf{r}, \mathbf{k} - \mathbf{k}') \tilde{u}_{\mathbf{k}'n'}(\mathbf{r}), \tag{31}$$

with

$$\tilde{v}_{\kappa}(\mathbf{r}, \mathbf{k} - \mathbf{k}') = \sum_{\mathbf{l}} \sum_{\mathbf{L}'} \frac{d\tilde{v}(\mathbf{r} + \mathbf{l})}{d\mathbf{R}_{\mathbf{L}'\kappa}} \times \frac{1}{|\{\mathbf{L}\}_{\kappa, \mathbf{r}}|} \sum_{\{\mathbf{L}\}_{\kappa, \mathbf{r}}} e^{i(\mathbf{k}' - \mathbf{k}) \cdot (\mathbf{r} + \mathbf{l} + \mathbf{L})}.$$
 (32)

 $\tilde{u}_{\mathbf{k}n}$ are the periodic parts of the pseudo wavefunctions and \mathbf{l} primitive lattice vectors used to define the supercell. The \mathbf{L} vectors are supercell lattices vectors, chosen, according to the minimal image convention, to minimize the distance between atom κ and the point $\mathbf{L} + \mathbf{r}$ in the neighboring supercell. Therefore the exponential in the previous equation is the phase factor needed to bring the primitive cells filling the supercell to the one at the origin. This downfolding produces $\mathbf{q} = \mathbf{k} - \mathbf{k}' \pmod{\mathbf{G}}$ dependent potential derivatives, but the accumulation over grid points used to compute the integrals is less demand-

ing than over the supercell. A more detailed description of this downfolding can be found in Ref. 20.

Notice that for polar materials, we remove the long-range part of the electron-phonon potential due to dipole interactions from the supercell before interpolation and then add it in the primitive cell at finite $\mathbf{q}^{20,37}$. See Appendix A.3 in Ref.²⁰.

The number of electron-phonon matrix elements to be computed may be reduced. Indeed, the relaxation times given by Eqs. 14, 15 and 16 involve delta functions. Therefore, to reduce the number of computations, we first evaluate the delta functions between all the selected bands at \mathbf{k} and \mathbf{k}' , and only if they are nonzero do we proceed to evaluate the electron-phonon matrix

elements. This optimization can only be done because in transport problems it is the relaxation time which is needed. It mimics the imaginary part of a self-energy. To obtain the real part as well, for example, using a Kramers-Kronig transform, the full set of states would be needed.

Once the electron-phonon matrix elements between ${\bf k}$ and ${\bf k}'$ have been obtained for the chosen states, the relaxation times are computed and stored for different temperatures, doping levels, number of bands or relaxation-time approximations and then the electron-phonon matrix elements are discarded. This way, we compute the transport coefficients for different settings in a single run of the code, where the electron-phonon matrix elements are computed just once.

TABLE I. Table of the materials considered. The reported values are obtained using the PBEsol exchange-correlation potential.

	lattice parameter [Å]	dielectric constant	Born effective charges	$\mathrm{Gap}\ [\mathrm{eV}]$
PbTe	a = 6.441	$\epsilon_r = 30.441$	$Z_{\rm Pb} = 5.876, Z_{\rm Te} = -5.876$	0.65
PbSe	a = 6.102	$\epsilon_r = 30.802$	$Z_{\rm Pb} = 4.601, Z_{\rm Se} = -4.601$	0.17
${ m Mg_2Si}$	a = 6.325	$\epsilon_r = 15.417$	$Z_{\rm Si} = -3.652, Z_{\rm Mg} = 1.826$	0.11
Mg_2Ge	a = 6.356	$\epsilon_r = 16.260$	$Z_{\text{Ge}} = -3.576, Z_{\text{Mg}} = 1.788$	0.08
Mg_2Sn	a = 6.739	$\epsilon_r = 18.775$	$Z_{\rm Sn} = -3.845, Z_{\rm Mg} = 1.922$	
NiTiSn	a = 5.865	$\epsilon_r = 23.511$	$Z_{\text{Ti}} = 2.771, Z_{\text{Sn}} = 1.179, Z_{\text{Ni}} = -3.950$	0.45
NiZrSn	a = 6.067	$\epsilon_r = 21.592$	$Z_{\rm Zr}=2.593,Z_{\rm Sn}=1.026,Z_{\rm Ni}=-3.619$	0.50
NiHfSn	a = 6.032	$\epsilon_r = 20.571$	$Z_{\rm Hf} = 2.682, Z_{\rm Sn} = 0.964, Z_{\rm Ni} = -3.645$	0.38

IV. THERMOELECTRIC MATERIALS

A. Computational details

In the following, we compute the transport properties of the materials listed in Tab. I. We consider several thermoelectric materials, including half-Heusler, rock-salts and antifluorites. The structures of those materials are described in the Supplemental Material³⁸. Transport properties are computed for doped compounds. The carrier concentrations we use are reported in Tab. II. They are taken from Hall measurements and used to determine the chemical potential according to Eq. 3.

All materials are computed with both the PBEsol³⁹ and PBE⁴⁰ exchange-correlation functionals using the VASP code^{22–26} and the PAW²¹ potentials listed in the Supplemental Material³⁸. A significant challenge arises with materials containing heavy elements, like PbTe and PbSe, where spin-orbit coupling (SOC) may be crucial. However, simply combining SOC with standard PBE or PBEsol functionals may results in an unphysical in-

verted gap⁴¹, leading to inaccurate transport properties. Therefore, for simplicity, SOC has been neglected in the present study. Accurately incorporating spin-orbit coupling necessitates the use of an exchange-correlation functional specifically designed for better band gap description. More details about the effects of spin-orbit coupling on transport properties are given in Appendix VI.

To obtain the electron-phonon interactions, different cells, which describe the same crystal structure, may be used to perform the steps listed in Sec. IIIB. We consider primitive, conventional, and supercells. They are generated from each other through simple matrix transformations. The basis vectors of the primitive cells are chosen as $(\frac{1}{2}(\mathbf{b}+\mathbf{c}),\frac{1}{2}(\mathbf{c}+\mathbf{a}),\frac{1}{2}(\mathbf{a}+\mathbf{b}))$, where $(\mathbf{a},\mathbf{b},\mathbf{c})$ are the basis vectors of the cubic conventional unit cells. Supercell are generated as multiple of the conventional cells. Details about the size of the supercells can be found in the Supplemental Material³⁸. For each compound, we consider two supercells to be able to check the convergence of the method with respect to the supercell size.

In this works, in step (a), the crystal structure is relaxed in the conventional unit cell and in step (b) dielectric constants and Born effective charges are computed using the primitive cell. In step (c), the atoms in the supercells are displaced using symmetrically irreducible displacements 10 of 0.03 Å.

For all compounds, the plane-wave cutoff energy is set to 400 eV. The sampling in reciprocal space, for Brillouin zone and supercell shape, are given in the tables of the Supplemental Material³⁸. The mesh number is roughly estimated by $10 \times |\mathbf{a}^*|$ where \mathbf{a}^* is a reciprocal basis vector of the cell used for the specific calculation, $\mathbf{a}^* \cdot \mathbf{a} = 2\pi$.

The long-range part of the electron-phonon potential needs to be considered. It is computed from a sum of G

vectors in reciprocal space (see Appendix A.3 of Ref. 20). We use a cutoff of 50 eV to perform this summation.

The lattice thermal conductivity is computed from phonon-phonon interaction calculations in the supercell approach, using phono3py^{42,43}, and solving the phonon Boltzmann equation under the relaxation-time approximation. Random directional displacements of 0.03 A were introduced in 120 supercells to compute anharmonic force constants using the symfc code⁴⁴. In Fig. 3, it is shown that sampling the Brillouin zone using a $30 \times 30 \times 30$ mesh is already sufficient to converge the lattice thermal conductivity.

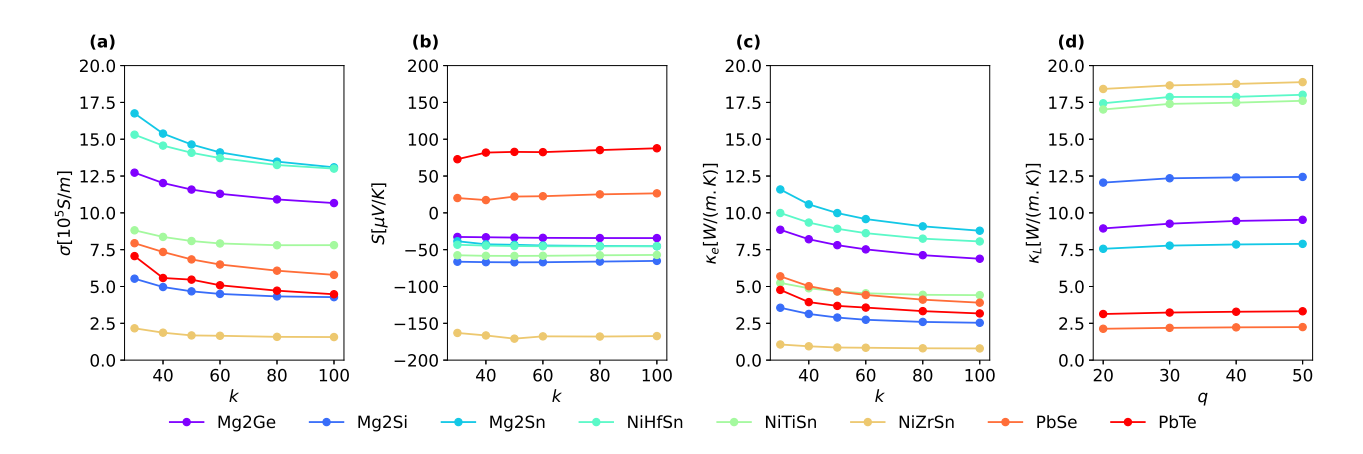


FIG. 3. Convergence of the (a) electronic conductivity (σ) , (b) thermopower (S), (c) electronic part of the thermal conductivity (κ_e) and (d) lattice part of the thermal conductivity (κ_L) , at 300 K, with respect to the sampling of the first Brillouin zone.

B. Results

The geometries of the materials were optimized using the PBEsol³⁹ and PBE⁴⁰ exchange-correlation functionals. The parameters we obtain are reported in Tab. I for the PBEsol functional, and in Tab. III, in Appendix A, for the PBE functional. For all compounds, we obtain smaller lattice parameters using the PBEsol exchange-correlation functional.

The electronic band structures are plotted in Appendix A along the paths given by Seekpath^{45,46}. Comparing the results obtained with the PBEsol and PBE exchange-correlation functionals, we do not see major topological changes in the band structure in the vicinity of the Fermi level. However, the values of the band gaps can be very different. For Mg₂Si, Mg₂Ge, PbTe and PbSe, the band gaps computed with the PBEsol functional are smaller than the ones obtained with PBE. For example, the PbSe band gap is strongly reduced using the PBEsol functional. This is due to a different parametrization of the exchange-correlation functional

which reduces the exchange contribution to the energy thus lowering the value of the band gaps⁴⁷. The opposite is observed for the half-Heusler, as the PBE gaps are smaller than those obtained from the PBEsol functional. The differences are small, however.

The phonon dispersions are shown in Appendix A for the PBEsol and PBE functionals. They are computed using the small supercells reported in the Supplemental Material³⁸. As already noted, the lattice parameters we obtain are smaller using the PBEsol exchange-correlation functional. Consequently, we obtain higher phonon frequencies. This is what we observe for NiTiSn, NiZrSn, NiHfSn, Mg₂Si, Mg₂Ge, PbTe. The change in the phonon spectrum is not a simple scaling of the frequencies, with larger differences being observed in the optical modes.

For Mg₂Sn and the PBE functional we find that the real space force-constants computed using symmetric displacements on the small $2 \times 2 \times 2$ supercell reported in the Supplemental Material³⁸ are insufficient to interpolate the phonon dispersion accurately as shown in Fig. 20 and hence we did not proceed with the calculation of the

transport coefficients in this case, reporting only the results for the $4\times4\times4$ supercell in Tab. II.

In Fig. 14, we show that in PbSe the optical modes at the zone center are very different for the PBE and PBEsol approximations. This is due to the different values for the dielectric function ϵ_r and Born effective charges Z_i as reported in Tab. I and Tab. III. When using the PBE ϵ_r and Z_i in the phonon calculation with PBEsol, the phonon dispersion becomes closer to the PBE one (Fig. 11). The same behavior is observed for the values of the transport properties for which we obtain $\sigma = 4.3 \, 10^5 (\Omega \text{m})^{-1}$, $S = 32.2 \, \mu \text{V/K}$, $\kappa_e = 2.9 \, \text{W/(m} \cdot \text{K})$, closer to the PBE results of Tab. II.

To compute the electronic transport properties, several parameters must be set to ensure the accuracy of $g(\mathbf{k}n, \mathbf{k}'n', \mathbf{q}j) \sim \langle \varphi_{\mathbf{k}n} | \partial \tilde{h}/\partial \mathbf{R} | \varphi_{\mathbf{k}'n'} \rangle \cdot \delta \mathbf{R}^{\mathbf{q}j}$. The planewave cutoff energy, E_{cut} , the number of points used to sample the Brillouin zone of the primitive cell, N_k , and the size of the supercell used to compute $g(\mathbf{k}n, \mathbf{k}'n', \mathbf{q}j)$ have to be carefully chosen for those calculations to be both efficient and accurate.

For all materials, to obtain the values of $E_{\rm cut}$ and N_k , we have converged the transport properties σ , S, and κ_e at T=300 K using the small supercells listed in the Supplemental Material³⁸ and the PBEsol functional. The Brillouin zone of the primitive cell is sampled using a uniform $k \times k \times k = N_k$ grid. Fig. 3 shows the result of these calculations with respect to k for $E_{\rm cut}=400$ eV. It can be seen that k=100 allows to obtain converged values, to 5 % accuracy, for all materials.

The derivatives of the Hamiltonian, $\partial \tilde{h}/\partial \mathbf{R}$, and the phonon spectra are obtained from supercell calculations which use $E_{\rm cut}=400$ eV. In the computation of $g(\mathbf{k}n,\mathbf{k}'n',\mathbf{q}j)$, this value defines the number of real-space grid points used to compute the integral $\langle \varphi_{\mathbf{k}n}|\partial \tilde{v}_{loc}/\partial \mathbf{R}|\varphi_{\mathbf{k}'n'}\rangle$. The transport properties we obtain are found to be almost insensitive to the value $E_{\rm cut}$ for values in the range 300-500 eV. To rationalize this result, it may be useful to notice that the largest suggested cutoff energy among the pseudopotentials we use is 310 eV for Ge.

We have also investigated the effect of the supercell size we use to compute the phonon spectra and $\partial \tilde{h}/\partial \mathbf{R}$. The results are reported in Tab. II for two supercell sizes for k=100 and $E_{\rm cut}=400$ eV. It is clear from this table that the electronic transport properties depend very weakly on the size of the supercell.

The lifetimes of holes or electrons are plotted in Figs. 4, 17 and 21 as functions of the Kohn-Sham energies. Two distinct behaviors are observed. In Fig. 4 the reciprocal lifetime closely follows the density of states and the transport function. This can easily be understood from Eq. 14 if the electron-phonon matrix elements are seen as constants, and the phonon energy is considered to be small. In Figs. 17 and 21, the reciprocal lifetime shows a minimum around the chemical potential. This can be understood from Eq. 14 as well. Assuming the electron-phonon matrix elements to be constant, and a

single energy $\hbar\omega$ in the phonon spectrum, we obtain

$$\frac{1}{\tau_{\mathbf{k}n}} \propto [n^0(\hbar\omega) + 1 - f^0(\epsilon_{\mathbf{k}n} - \hbar\omega)]\rho(\epsilon_{\mathbf{k}n} - \hbar\omega) + [n^0(\hbar\omega) + f^0(\epsilon_{\mathbf{k}n} + \hbar\omega)]\rho(\epsilon_{\mathbf{k}n} + \hbar\omega).$$

If, moreover, the density of states is almost constant around $\epsilon_{\mathbf{k}n}$, then

$$\frac{1}{\tau_{\mathbf{k}n}} \propto [2n^0(\hbar\omega) + 1 - f^0(\epsilon_{\mathbf{k}n} - \hbar\omega) + f^0(\epsilon_{\mathbf{k}n} + \hbar\omega)] \times \rho(\epsilon_{\mathbf{k}n}).$$

The factor in the square bracket takes the value $2n^0(\hbar\omega) + 1$ for energies far from the chemical potential, but has a pronounced minimum of depth $\tanh(\hbar\omega)/(2k_BT)$ at the chemical potential. Its width is about $\pm\hbar\omega$ around the chemical potential. This is the behavior observed in Figs. 17 and 21. Fig. 4 can also be recovered if the phonon frequency $\hbar\omega$ is assumed to be small. The Fermi functions can be neglected and therefore

$$\frac{1}{\tau_{\mathbf{k}n}} \propto \rho(\epsilon_{\mathbf{k}n}).$$

Looking at the values of the dips in the lifetimes of Figs. 17 and 21, we locate the effective phonon frequencies ω in the acoustic part of the phonon spectra. The values are lower for half-Heusler than for the Mg₂X compounds, and even lower for the rocksalt compounds. Therefore, as anticipated, the effective phonon frequency decreases as the mass of the compound increases.

The result in Fig. 3 suggests that above room temperature we can obtain an acceptable estimation of the thermoelectric figure of merit using a $60 \times 60 \times 60$ mesh in the first Brillouin zone. We use the PBEsol exchange-correlation functional. The results are shown in Fig. 7, and in Figs. 18 and 22 in Appendix A.

To understand the thermoelectric figure of merit as a function of temperature, we write

$$ZT = (ST)^2 \left(\frac{\sigma}{\kappa T}\right),$$
 (33)

$$= (ST)^2 \left(\frac{\sigma T}{\kappa_e}\right) \left(\frac{1}{1 + \frac{\kappa_L}{\kappa_e}} \frac{1}{T^2}\right). \tag{34}$$

As shown in Fig. 5, the first factor in the above formula is a strongly increasing function of the temperature, roughly as T^4 because of Mott's law.

In Figs. 5, 7, 18 and 22, we observe that the agreement between theory and experiment is roughly correct for the thermopower. The compounds we consider, and thermoelectric compounds in general, are highly doped. Therefore, to compute σ , S and κ_e , one should add the scattering rate of electrons on impurities to the electron-phonon scattering rate to obtain the total relaxation time. One could for example, add those two scattering mechanisms using Matthiesen rule. However, the thermopower S is known to depend weakly on the relaxation time. Indeed,

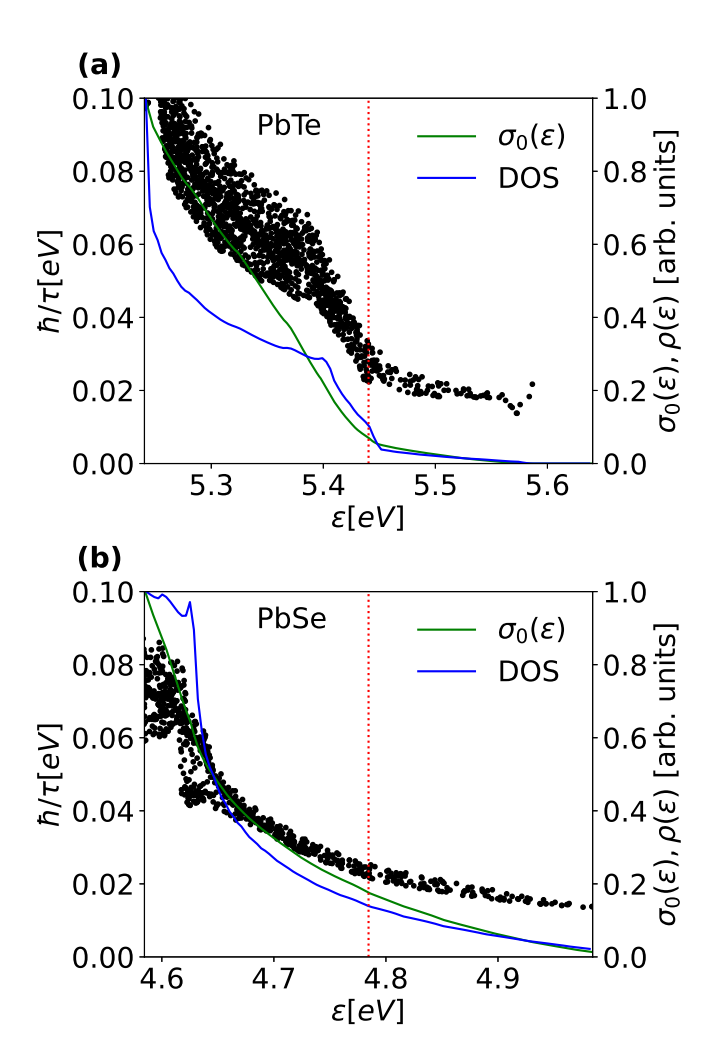


FIG. 4. Reciprocal lifetimes, \hbar/τ , at 300 K, as function of the band energies, are shown as black dots for (a) PbTe and (b) PbSe. The PBEsol exchange correlation functional is used. The transport function at constant relaxation time, $\sigma_0(\epsilon)$, and the density of states, $\rho(\epsilon)$, in arbitrary units, are shown as green and blue curves, respectively. The chemical potential is shown using a red dotted line. PbTe and PbSe are p doped compounds in our calculations (see Tab. II), therefore it is the lifetime of hole which is plotted.

it is the ratio of two Onsager coefficients (Eq. 26), and some cancellations between the numerator and the denominator occur. Therefore, the moderate agreement observed between theory and experiment in Figs. 5, 7, 18 and 22 for the thermopower cannot entirely be explained by a too approximate relaxation time. The doping is so strong in those compounds that the electronic structure itself may be modified around the chemical potential and impact the thermopower. For example, in the FeVSb half-Heusler, it is well known that, around the chemical potential, the electronic structure is strongly modified by doping ⁵⁶.

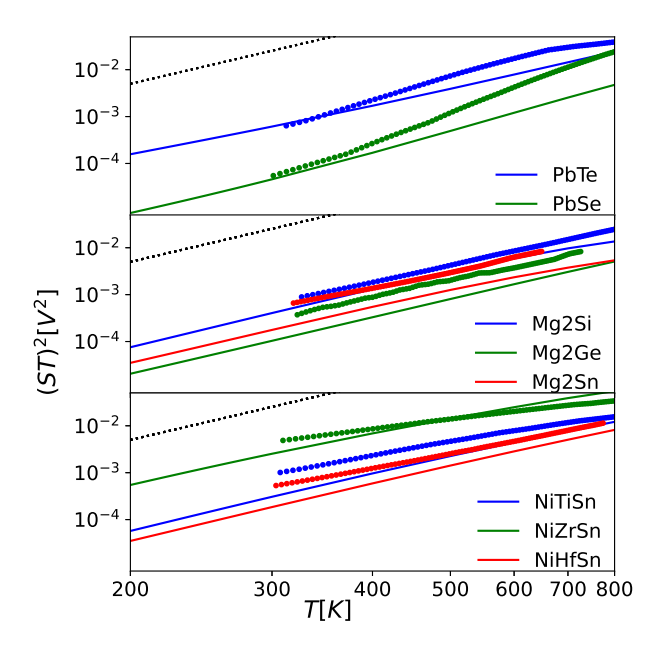


FIG. 5. $(ST)^2$ as a function of temperature. The calculations are shown as continuous lines and experimental measurements ^{48–55} as filled circles. The T^4 law is shown as a black dotted line.

The second factor in Eq. 34, $\sigma T/\kappa_e$ is approximately independent of temperature and is given by the inverse of the Lorenz number, $L_0 = 2.44 \, 10^{-8} \, \text{V}^2 \text{K}^{-2}$, if the metallic regime is reached and the temperature is low enough. This factor is shown in Fig. 8. We observe that at T=0K it reaches the theoretical limit L_0 , but in the operating temperature range 200 - 800 K, on average it takes a lower value. In models with parabolic bands and a power-law relaxation time^{57–59} such low values can be obtained when the density of state is rapidly changing which coincides with large absolute values of the Seebeck coefficient. The rise of the Lorenz number above the Wiedemann-Franz value, L_0 , at high temperature, indicates multiband effects^{59,60}. Notice that the convergence with respect to k of the reported transport properties has been studied at 300 K. Therefore, the values below that temperature are only indicative, the main purpose of reporting them is to show that at T = 0 K the Wiedemann-Franz value L_0 is reached, as a measure of the quality of our numerical scheme.

The last factor in Eq. 34 measures the ratio of the lattice to electronic thermal conductivity. If we use the high-temperature limit of the electron-phonon lifetime, $\hbar/\tau_{ep}=2\pi\lambda k_BT$, with λ the electron-phonon coupling constant^{19,61}, then the lifetime is inversely proportional to the temperature, and the electronic thermal conductivity becomes independent of temperature. It is obviously a gross approximation, because, for example, at high enough temperature the electronic thermal conductivity increases due to multiband effects⁶², as shown in

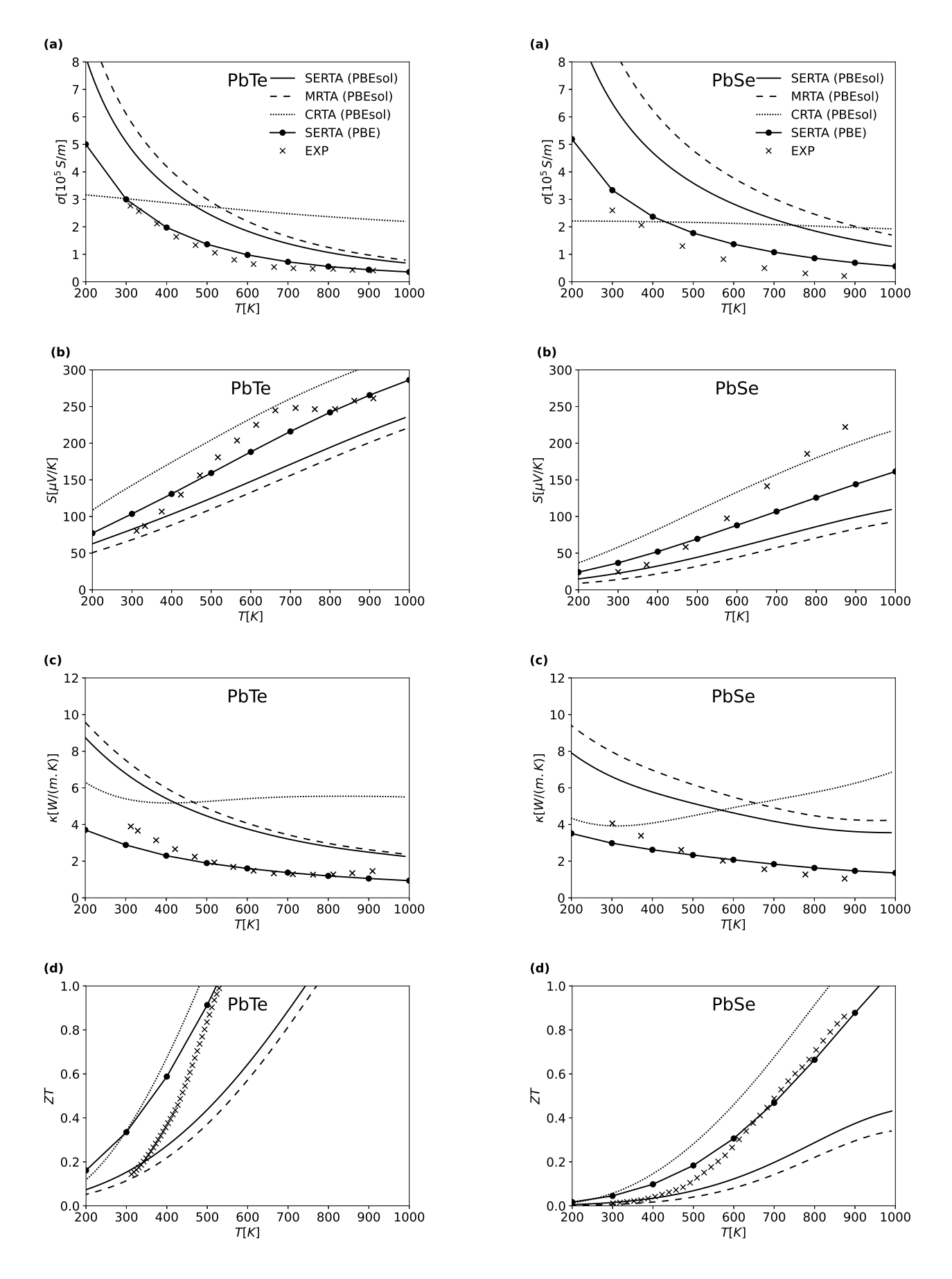


FIG. 6. Transport properties of PbTe computed with PBEsol and k=60. (a) electronic conductivity σ , (b) thermopower S, (c) thermal conductivity κ and (d) ZT thermoelectric figure of merit. Experimental measurements⁴⁸ are shown using crosses. The results of computations are shown using continuous, dashed and dotted lines for the SERTA, MRTA and CRTA approximations, respectively. For the CRTA, $\tau=10^{-14}\,\mathrm{s}$ is used. To compute the lattice thermal conductivity q=27 is used.

FIG. 7. Transport properties of PbSe computed with PBEsol and k=60. (a) electronic conductivity σ , (b) thermopower S, (c) thermal conductivity κ and (d) ZT thermoelectric figure of merit. Experimental measurements⁴⁹ are shown using crosses. The results of computations are shown using continuous, dashed and dotted lines for the SERTA, MRTA and CRTA approximations, respectively. For the CRTA, $\tau=10^{-14}\,\mathrm{s}$ is used. To compute the lattice thermal conductivity q=28 is used.

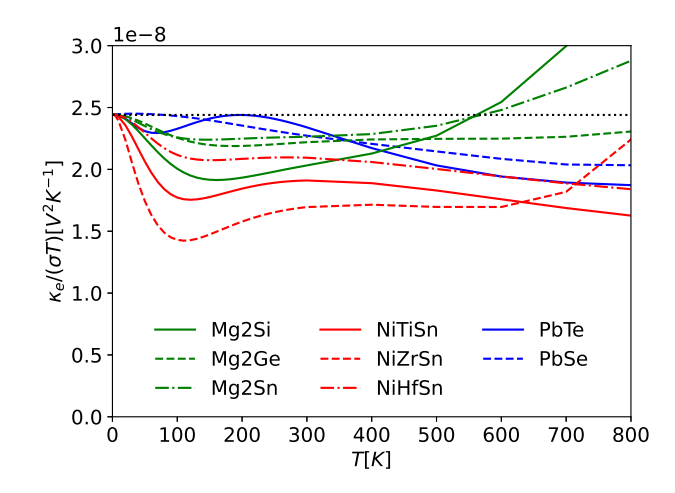


FIG. 8. The Lorenz function $\kappa_e/(\sigma T)$ as a function of temperature.

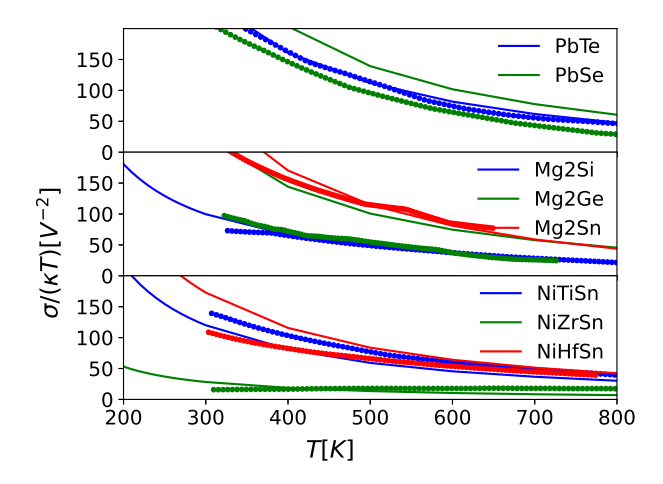


FIG. 9. $\sigma/(\kappa T)$ as a function of temperature. The calculations are shown as continuous lines and experimental measurements $^{48-55}$ as filled circles.

Fig. 22. Nevertheless, if we use this approximation and because $\kappa_L \approx C/T^{\delta}$ with $\delta \approx 1$, then we obtain that the last factor in Eq. 34 decreases with temperature as $1/(T^2 + cT)$, and therefore much slower than $(ST)^2$.

Because experimentally it is difficult to split κ into κ_e and κ_L , to compare with theory, in Fig. 9 we show the product of the last two factors of Eq. 34, $\sigma/(\kappa T)$. According to the above analysis, it behaves as $1/(T^2+cT)$ with temperature. As in the case of $(ST)^2$, the agreement with experiment is roughly correct. The results of Fig. 5 and Fig. 9 can be combined, in Fig 10, to obtain the figure of merit as a function of temperature. The results are also replotted individually for each compound family in Figs. 7, 18 and 22. It is observed that the ZT follow approximately a T^2 law, as obtained from the above analysis.

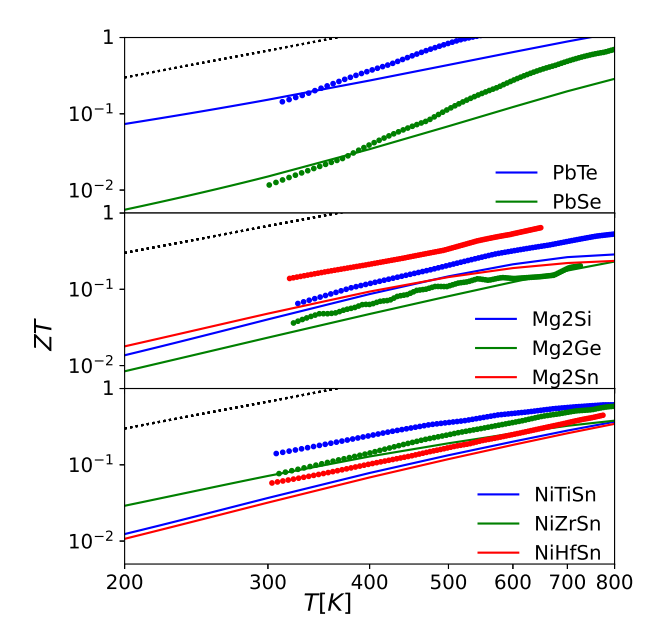


FIG. 10. ZT as a function of temperature. The calculations are shown as continuous lines and experimental measurements $^{48-55}$ as filled circles. The T^2 law is shown as a black dotted line.

This reasonable agreement between theory and experiment should be considered with caution. If we look more into the details, in Tab. II, but also in Figs. 7, 18 and 22, where σ and κ are plotted separately, then we see that the agreement with experiment indicates room for improvement. As previously mentioned, we may attribute, at least partially, the difference between theory and experiments to impurities. In κ_L , the impurities would manifest themselves through a relaxation time due to the scattering of the phonons on mass fluctuations⁶³, and in κ_e through the scattering of the electrons on the change in the potential due to doping. It seems that those two effects partially cancel in the ratio κ_L/κ_e , which allows us to obtain a rough estimate of the thermoelectric figure of merit, in Fig. 10, considering only the electron-phonon interaction.

In Figs. 7, 18 and 22, we considered the different relaxation-time approximations given by Eq. 14 and Eq. 15. The trends we observe are the same and therefore the above conclusions still apply. Moreover, it can be noted that for the conductivity we have MRTA > SERTA.

From Tab. II and Fig. 7 we observe that the agreement of electrical conductivity with experiment is better for PbTe than for other compounds, and in fact even improved if we use the PBE exchange-correlation functional instead of PBEsol (See Fig. 7). This, however, may be accidental since impurity scattering is neglected.

Finally, we mention a peculiar behavior in Fig. 10. The increase of ZT with temperature for PbTe and PbSe,

given by the experiments in Ref. 48 and 49 seems to be faster than those given by the calculations and experiments on other materials. This behavior is also observed in the thermopower in Fig. 5, and therefore is likely due to an electronic effect. It could be due to the temperature dependence of the electronic structure, as mentioned in Ref. 64 , or due to changes in the electronic structure due to doping.

C. Discussion

In this paper we have considered the transport properties of thermoelectric compounds. Those compounds are heavily doped compounds containing heavy elements, therefore it is interesting to discuss how impurity scattering and spin orbit coupling may impact the results.

The scattering of electrons on impurities is not yet implemented in our approach, therefore direct comparison with experiments is difficult. Indeed, in the previous sections we have presented the results without accounting for this contribution. However, using the model of Debye and Conwell⁶⁵ it is possible to get an estimate of how strongly impurity scattering impact the electrical conductivity at a given impurity concentration. In Appendix V we reproduce the results of 66 and 67 for n-type silicon and describe the model. The agreement with experiments is excellent as long as impurity scattering is included using the above mentioned model. Figs. 23 and 24 evidence that for heavy doping $(n \sim 10^{19} \, cm^{-3})$ impurity scattering is essential to consider, even at room temperature. This is in this concentration range that thermoelectric compounds usually operate, as seen in Tab. II. Therefore we applied the same empirical model to the compounds considered in this study. The results are shown in Fig. 11. According to Eq. 3, the electrical conductivity we obtain from our ab initio calculations (σ_{ep}) is multiplied by the Debye and Conwell⁶⁵ factor $(1+X^2[\operatorname{ci}(X)\cos(X)+\operatorname{si}(X)\sin(X)])$ to account for impurity scattering. Notice that in this case to compute $X = \sqrt{6\sigma_{ep}/\sigma_{ei}}$ we use the Brooks-Herring formula⁶⁸ for the electrical conductivity σ_{ei} corresponding to impurity scattering only, since an empirical formula equivalent to Eq. 4 for Si is not available for the compounds we consider. We see on Fig. 11 that we obtain a good agreement with experiments. One exception is Mg₂Sn, but it has been noted already that the PBEsol and PBE functionals give a negative band gap, therefore the discrepancy with experiments is likely to be due to the too approximate electronic structure we use.

As mentioned already, spin-orbit coupling (SOC) was not considered in those calculations because at the level of semi-local functionals it may not lead to a systematic improvement of the transport properties. Indeed, it is shown in⁴¹ that for band gaps, at the level of semi-local functionals, including SOC is not always beneficial. This is also discussed in⁶⁹ for the effective mass. In Appendix

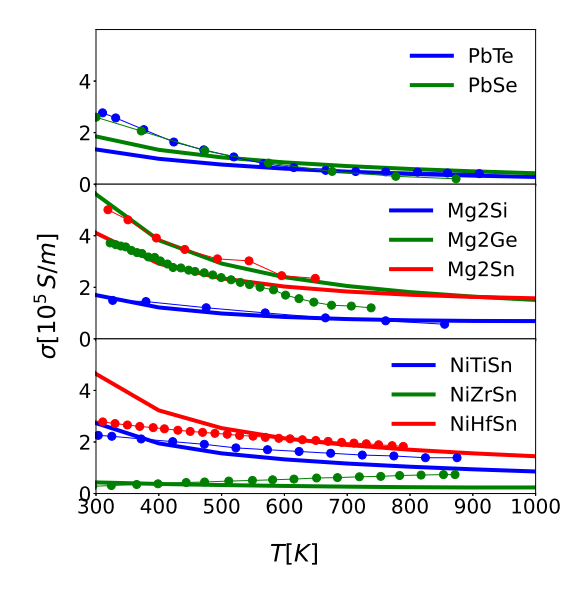


FIG. 11. Electrical conductivity of the thermoelectric compounds considered in this work. The results of the calculations are shown as continuous lines, and the experimental values as dots. The calculations include impurity scattering as given by the Debye and Conwell formula. NiXSn and Mg₂X have been computed using the PBEsol exchange correlation functional using parameters discussed explicitly in the previous sections while the PBE functional is used for PbX compounds. Experimental values are obtain from the references given in Tab. II.

VI we confirm this behaviour for the electrical conductivity considering PbSe as a special case.

We end this section discussing the impact of carrier concentration on our results. Our approach to compute the transport coefficients assumes the doping is weak enough for bands to exists and the Boltzmann equation to hold. The Boltzmann equation, Eq. 6, is written using the electron band structure $\epsilon_{\mathbf{k}n}$ of the perfect crystal. Therefore to obtain the heat flux, $(\epsilon_{\mathbf{k}n} - \mu)\mathbf{v}_{\mathbf{k}n}f_{\mathbf{k}n}$, the chemical potential is computed from Eq. 3 with $\rho(\epsilon)$ the density of states of the perfect crystal. To obtain the value of μ at a given temperature Eq. 3 is solved considering the carrier concentration n_0 as an input parameter. In this work we have assumed that n_0 can be obtained from Hall measurements and is equal to the Hall number n_H given in Tab. II. This is the approach used in most works, but it is an approximation. At first n_H equals the carrier concentration only for a spherical Fermi surface³⁰. But, in fact, n_0 does not even need to equal the carrier concentration. It should be regarded as an effective parameter used to locate the chemical potential which properly selects the states which carry the currents. In Eq. 3 if $\rho(\epsilon)$ is the density of the real crystal, then obviously n_0 is the carrier concentration. But in our approach $\rho(\epsilon)$ is the density of the perfect crystal, therefore n_0 contains implicit information about the

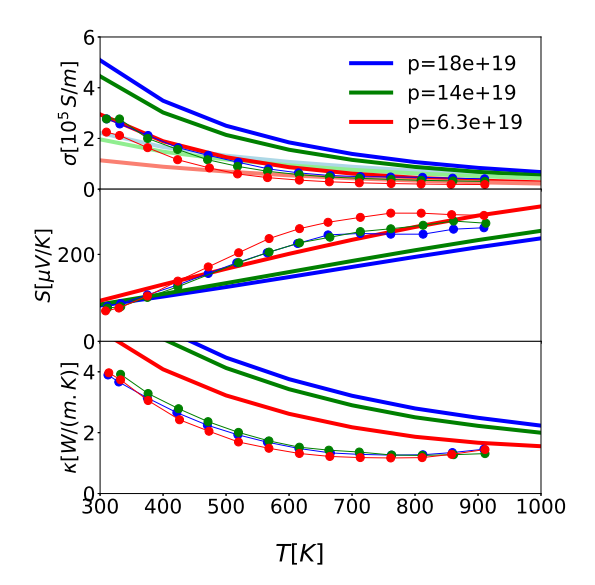


FIG. 12. Transport properties of PbTe for different carrier concentrations. Calculations are shown as continuous lines and experiments as dots. Calculations are performed using the PBEsol functional in the SERTA approximation. Experiments are from⁴⁸. The light blue green and red lines for the conductivity show the results of the calculations corrected for impurity scattering using the Debye and Conwell⁶⁵ formula.

change of the density of states due to the doping and the microstructure of the sample. We do not have a procedure to choose n_0 accurately, therefore we regard $n_0 \approx n_H$ as a practical approximation. In Fig. 12 we computed the transport properties of PbTe for the different Hall concentrations reported in 48 . The change of the transport properties with carrier concentration reproduce well the experiments, and once the conductivity is corrected for impurity scattering the agreement is excellent. This is an interesting result because it can be seen from the band structure and from ⁷⁰ that, despite a complicated, non-spherical Fermi surface, the deviation between n_0 and n_H still allows for a reasonable calculation of the transport properties. As reported in 48, at large doping concentration, 18×10^{19} cm⁻³, n-type intrinsic defects are created when the Na doping atoms are entering the lattice. Therefore, the n_H value obtained experimentally characterizes a complicated microstructure. At a given temperature, the same n_H value can be obtained for different microstructures; our approach does not allow us to distinguish between them. Therefore, whether or not the electronic states selected by the chemical potential approximately describe the electronic states of the actual sample is assessed by comparing the computed transport properties to the experiments. In Fig. 12, for $p = 18 \times 10^{19}$ cm⁻³, we observe that despite the rather complicated microstructure, and the known convergence of the L and Σ bands due to doping⁴⁸, the agreement with experiment is acceptable when impurity

scattering is taken into account.

V. CONCLUSIONS

We propose a computational approach to the thermoelectric figure of merit based on the calculation of the electron-phonon and phonon-phonon interactions from first-principles. Numerical strategies have been developed to make these calculations efficient. In particular, we show that the transport coefficients can be computed without any interpolation of the electronphonon matrix elements, other than the minimal image convention^{18–20,71}. Avoiding the Wannierization procedure, which often requires human intervention, facilitates the direct application of this approach to large sets of materials under different physical conditions such as strain or using different exchange-correlation functionals.

The transport coefficients we obtain reproduce the experiments, even if the agreement is not perfect. A better description of the electronic structure such as band gaps and effective masses is required to reduce the discrepancies. This, in turn, is also expected to be important in the description of the long-range part of the electron phonon potential since the value of the band gap also affects the value of the dielectric tensor and Born effective charges and we have seen in Sec. IVB that those quantities strongly impact the transport properties. But of course a better description of the band gaps should not come at the expense of a good description of the effective masses 72, since those are also crucial for the computation of the transport coefficients.

For the heavily doped conditions of the systems under study, we have seen that the inclusion of impurity scattering and the band structure relaxation should have a non-negligible impact on the final results. Additional work should also be done to investigate the role of the lattice thermal expansion as well as the effect of the temperature dependence of the band-structure in the electronic transport coefficients.

ACKNOWLEDGMENTS

This work was supported by JSPS KAKENHI Grant Numbers JP24K08021, JP24H00190, JP25H01246, and 25H01252. Part of the calculations in this study were performed on the Numerical Materials Simulator at NIMS.

TABLE II. Table of thermoelectric transport properties at room temperature. Negative n values mean p doping. The units are $n[10^{19} \, \mathrm{cm}^{-3}]$, $\sigma[10^5 \, (\Omega \cdot \mathrm{m})^{-1}]$, $S[10^{-6} \, \mathrm{V/K}]$, $\kappa[\mathrm{W/(m \cdot K)}]$. A $100 \times 100 \times 100$ mesh is used to sample the Brillouin zone to compute the electronic transport properties. To compute the total thermal conductivity (κ) of large supercells, we used the value of the lattice thermal conductivities of the small supercells. The mesh sizes used to sample the Brillouin zone to compute the lattice thermal conductivities are given in Figs. 7, 18 and 22. The *information* column contains the experimental nominal composition, or the supercell size, of the conventional cells, used for the calculation.

	n	σ	S	κ	κ_e	κ_l	ZT	method	
PbTe	-18	2.9	76	4			0.12	exp	$Pb_{0.96}TeNa_{0.04}^{48}$
	-18	4.5	87.7	6.4	3.2	3.2	0.16	PBEsol	
	-18	4.4	86.8	6.3	3.1		0.16	PBEsol	$4 \times 4 \times 4$
	-18	2.6	109.8	2.6	1.7	0.9	0.36	PBE	$2 \times 2 \times 2$
	-18	2.6	109.5	2.6	1.7		0.36	PBE	$4 \times 4 \times 4$
PbSe	-16	2.6	24.3	2.4			0.02	\exp	$Pb_{0.985}SeK_{0.015}^{49}$
	-16	5.8	26.5	6.1	3.9	2.2	0.02	PBEsol	$2\times2\times2$
	-16	5.6	26.5	6.0	3.8		0.02	PBEsol	$4 \times 4 \times 4$
	-16	2.9	40.4	2.7	1.9	0.8	0.05	PBE	$2 \times 2 \times 2$
	-16	2.9	40.8	2.7	1.9		0.05	PBE	$4 \times 4 \times 4$
Mg_2Si	15	1.5	-88	6.7			0.05	exp	$\mathrm{Mg2SiSb_{0.02}}^{50}$
	15	4.3	-65.2	14.8	2.5	12.3	0.04	PBEsol	$2 \times 2 \times 2$
	15	4.1	-65.0	14.8	2.5		0.04	PBEsol	$4 \times 4 \times 4$
	15	3.7	-79.5	14.2	2.3	11.9	0.05	PBE	$2 \times 2 \times 2$
	15	3.6	-79.4	14.1	2.2		0.05	PBE	$4 \times 4 \times 4$
${\rm Mg_2Ge}$	46	4	-59	12			0.03	\exp	$\rm Mg_{2.2}Ge_{0.995}Sb_{0.005}{}^{51}$
	46	10.6	-34.2	16.1	6.9	9.2	0.02	PBEsol	$2 \times 2 \times 2$
	46	10.3	-34.1	15.8	6.6		0.02	PBEsol	$4 \times 4 \times 4$
	46	9.6	-40.1	14.7	6.2	8.5	0.03	PBE	$2 \times 2 \times 2$
	46	9.3	-40.0	14.5	6.0		0.03	PBE	$4 \times 4 \times 4$
${ m Mg_2Sn}$	44.5	4.9	-78	7.4			0.12	\exp	$Mg2Sn_{0.98}Sb_{0.02}^{52}$
	44.5	13.1	-45.4	16.5	8.8	7.7	0.05	PBEsol	$2 \times 2 \times 2$
	44.5	12.7	-45.4	16.2	8.5		0.05	PBEsol	$4 \times 4 \times 4$
	44.5					6.0		PBE	$2 \times 2 \times 2$
	44.5	15.2	-35.4	15.7	9.7		0.04	PBE	$4 \times 4 \times 4$
NiTiSn	72	2.2	-102	5.3			0.13	\exp	${ m Ti}_{0.975}{ m Ta}_{0.025}{ m NiSn}^{53}$
	72	7.8	-57.1	21.8	4.4	17.4	0.03	PBEsol	$2 \times 2 \times 2$
	72	7.8	-57.1	21.8	4.4		0.03	PBEsol	$4 \times 4 \times 4$
	72	7.0	-60.3	18.8	4.0	14.8	0.04	PBE	$2 \times 2 \times 2$
	72	7.0	-60.3	18.8	4.0		0.04	PBE	$4 \times 4 \times 4$
NiZrSn	5.9	0.28	-224	6.1			0.07	\exp	$\rm ZrNiSn^{54}$
	5.9	1.6	-167.3	19.4	0.8	18.6	0.07	PBEsol	$2 \times 2 \times 2$
	5.9	1.6	-167.3	19.4	0.8		0.07	PBEsol	$4 \times 4 \times 4$
-	5.9	1.4	-174.6	17.4	0.7	16.7	0.07	PBE	$2\times2\times2$
	5.9	1.4	-174.6	17.4	0.7		0.07	PBE	$4 \times 4 \times 4$
NiHfSn							0.05	_	
						17.8	0.03	PBEsol	$2\times2\times2$
	72.3	12.9	-45.2	25.8	8.0		0.03	PBEsol	$4 \times 4 \times 4$
	72.3	12.0	-47.4	22.6	7.4	15.2	0.04	PBE	$2 \times 2 \times 2$
	72.3	11.9	-47.4	22.6	7.4		0.04	PBE	$4 \times 4 \times 4$

Appendix A: Thermoelectric materials

The materials properties we obtained are summarized in Tab. I when the PBEsol exchange correlation potential is used, and in Tab. III for PBE.

TABLE III. Table of the materials considered. The reported values are obtained using the PBE exchange-correlation potential.

	lattice parameter [Å]	dielectric constant	Born effective charges	Gap [eV]
PbTe	a = 6.566	$\epsilon_r = 26.400$	$Z_{\rm Pb} = 5.730, Z_{\rm Te} = -5.730$	0.83
PbSe	a = 6.216	$\epsilon_r = 20.213$	$Z_{\rm Pb} = 4.797, Z_{\rm Se} = -4.797$	0.44
Mg_2Si	a = 6.360	$\epsilon_r = 15.365$	$Z_{\rm Si} = -3.702, Z_{\rm Mg} = 1.851$	0.21
Mg_2Ge	a = 6.411	$\epsilon_r = 16.851$	$Z_{\text{Ge}} = -3.650, Z_{\text{Mg}} = 1.825$	0.16
${ m Mg_2Sn}$	a = 6.808	$\epsilon_r = 20.552$	$Z_{\rm Sn} = -3.938, Z_{\rm Mg} = 1.969$	
NiTiSn	a = 5.945	$\epsilon_r = 24.382$	$Z_{\text{Ti}} = 2.814, Z_{\text{Sn}} = 1.122, Z_{\text{Ni}} = -3.936$	0.44
NiZrSn	a = 6.147	$\epsilon_r = 22.047$	$Z_{\rm Zr}=2.653,Z_{\rm Sn}=0.955,Z_{\rm Ni}=-3.608$	0.48
NiHfSn	a = 6.113	$\epsilon_r = 21.067$	$Z_{\rm Hf} = 2.735, Z_{\rm Sn} = 0.892, Z_{\rm Ni} = -3.627$	0.37

1. Rocksalt

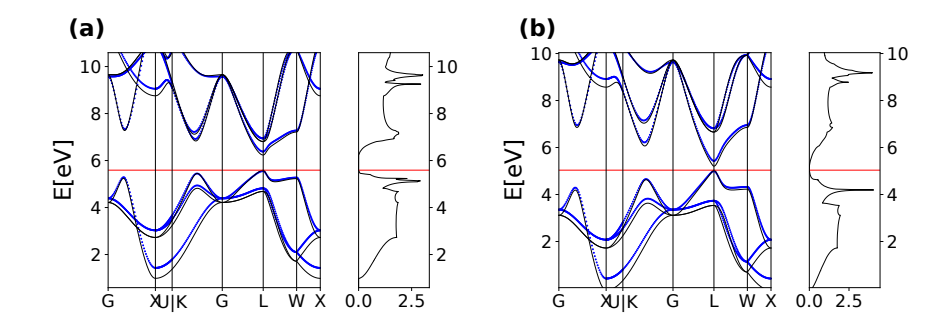


FIG. 13. Electron band structures of (a) PbTe and (b) PbSe using the PBEsol exchange-correlation functional, in black and PBE in blue.

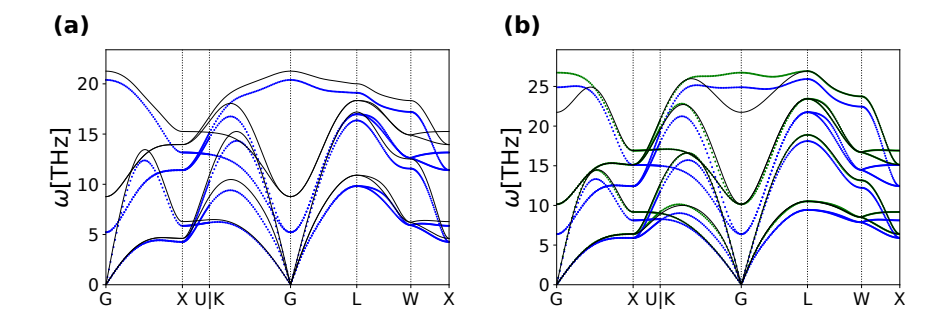


FIG. 14. Phonon dispersion of (a) PbTe and (b) PbSe using the PBEsol exchange-correlation functional, in black and PBE in blue. In (b) the PBEsol dispersion obtained using the PBE dielectric function and Born effective charges is also shown in green (see main text).

2. Half Heusler

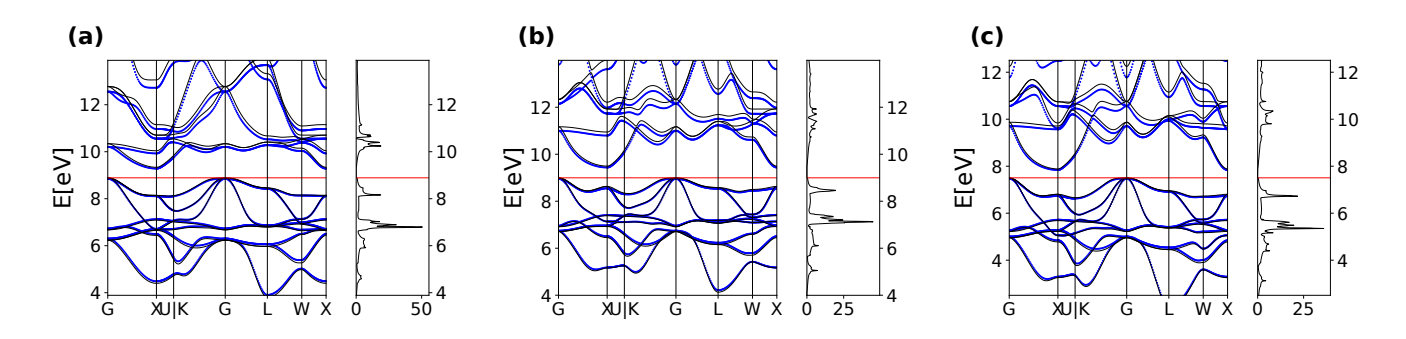


FIG. 15. Electron band structures of (a) NiTiSn, (b) NiZrSn and (c) NiHfSn using the PBEsol exchange-correlation functional, in black and PBE in blue.

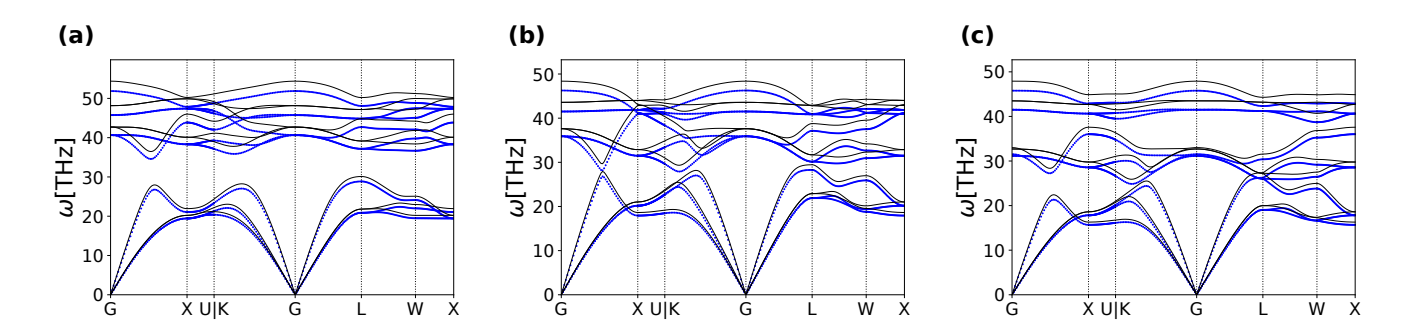


FIG. 16. Phonon dispersion of (a) NiTiSn, (b) NiZrSn and (c) NiHfSn using the PBEsol exchange-correlation functional, in black and PBE in blue.

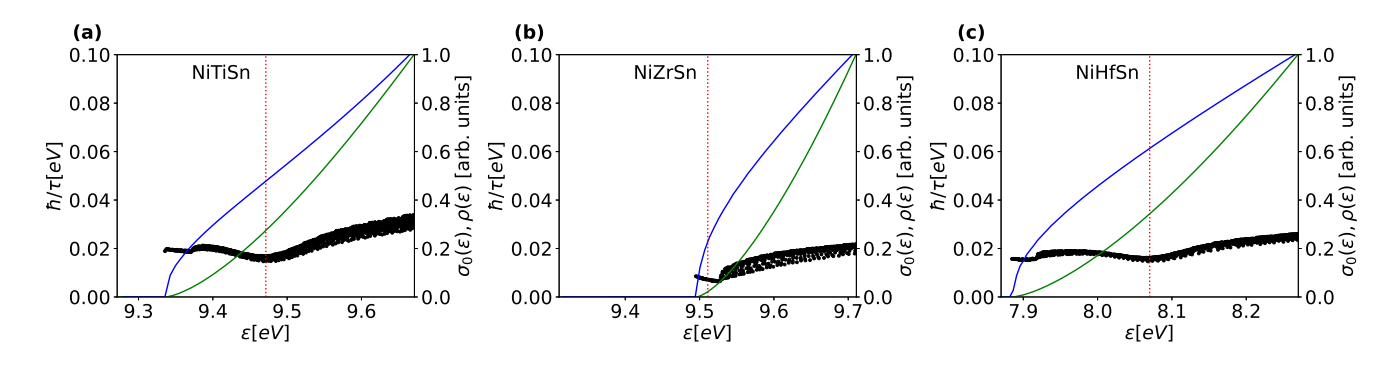


FIG. 17. Reciprocal lifetimes, \hbar/τ , at 300 K, as function of the band energies, are shown as black dots for (a) NiTiSn, (b) NiZrSn and (c) NiHfSn. The PBEsol exchange correlation functional is used. The transport function at constant relaxation time, $\sigma_0(\epsilon)$ is shown in green, the density of states, $\rho(\epsilon)$, in blue. Arbitrary units are used. The chemical potential μ is shown using a vertical red dotted line.

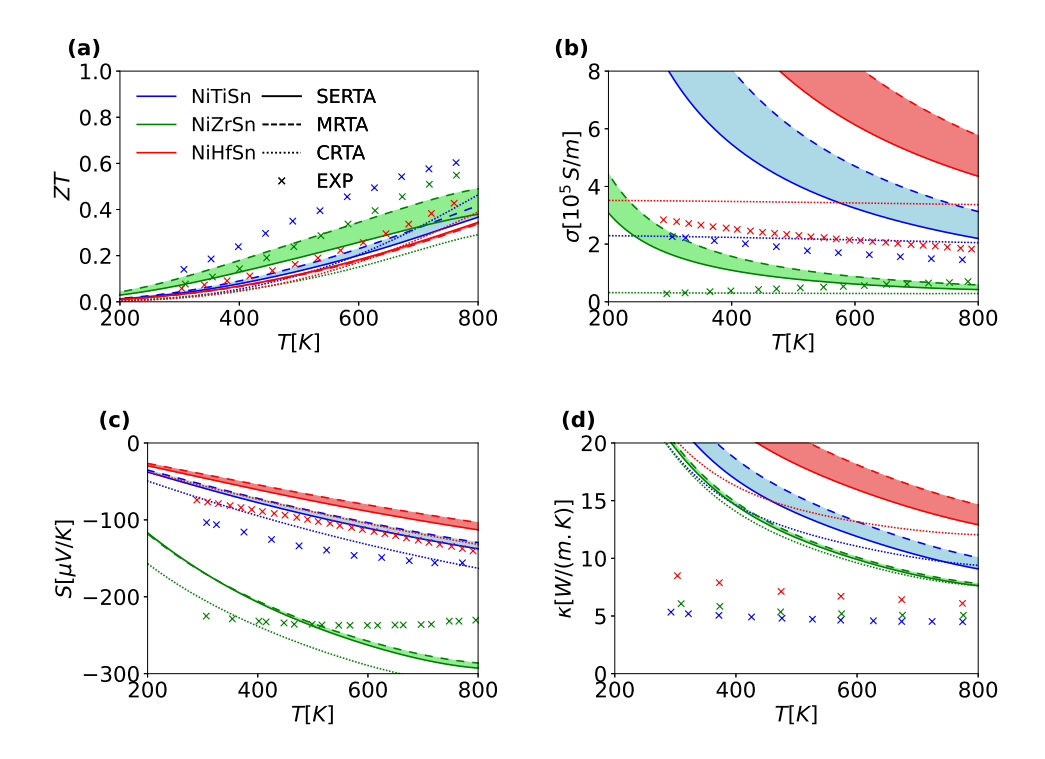


FIG. 18. Transport properties of half Heusler compounds computed with PBEsol. (a) ZT thermoelectric figure of merit, (b) electronic conductivity σ , (c) thermopower S, and (d) thermal conductivity κ . A k=60 mesh sampling is used. Experimental measurements^{53–55} are shown using crosses. The results of computations are shown using continuous, dashed and dotted lines for the SERTA, MRTA and CRTA approximations, respectively. For the CRTA, $\tau=10^{-14}\,\mathrm{s}$ is used. To compute the lattice thermal conductivity, a sampling of q=30, q=29 and q=29 are used for NiTiSn, NiZrSn and NiHfSn respectively. For each compound, the differences between SERTA and MRTA approximations are shown using shaded areas.

3. Mg₂Si, Mg₂Ge and Mg₂Sn

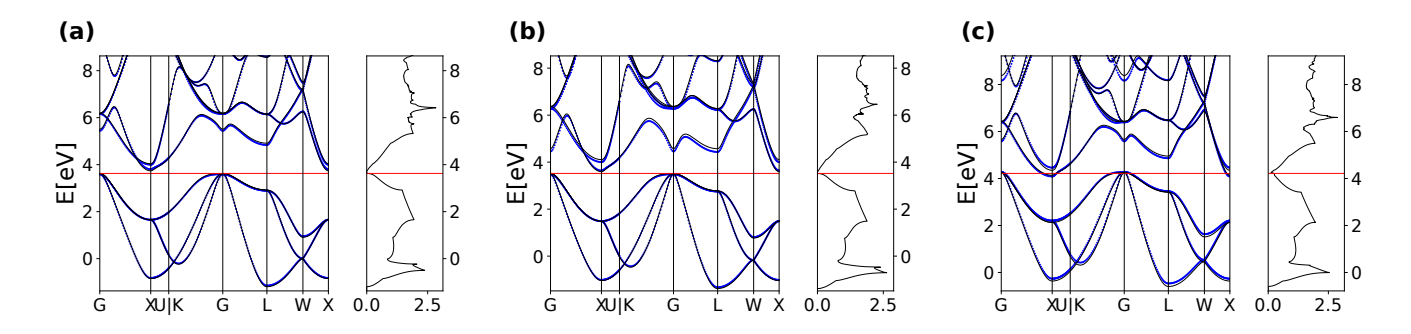


FIG. 19. Electron band structures of (a) Mg_2Si , (b) Mg_2Ge and (c) Mg_2Sn using the PBEsol exchange-correlation functional, in black and PBE in blue.

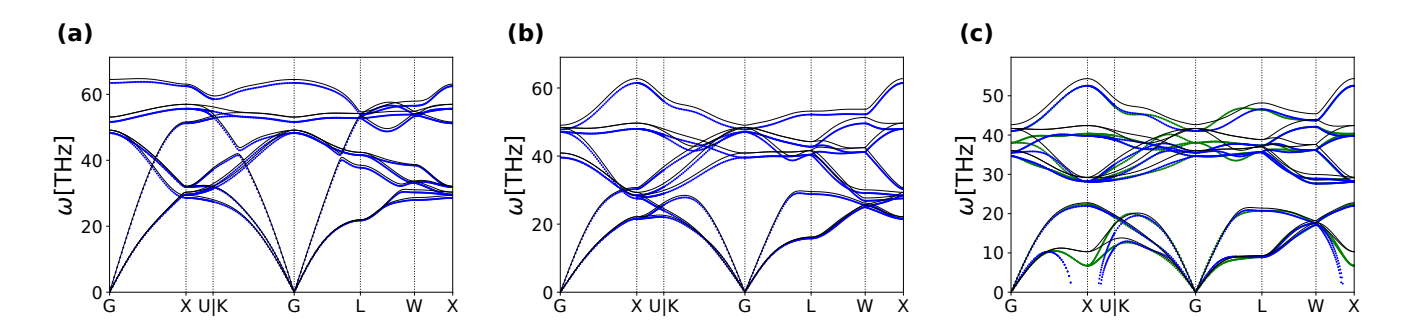


FIG. 20. Phonon dispersion of (a) Mg_2Si , (b) Mg_2Ge and (c) Mg_2Si using the PBEsol exchange-correlation functional in black and PBE in blue. In (c) the PBE dispersion obtained using a $4 \times 4 \times 4$ supercell is also shown in green.

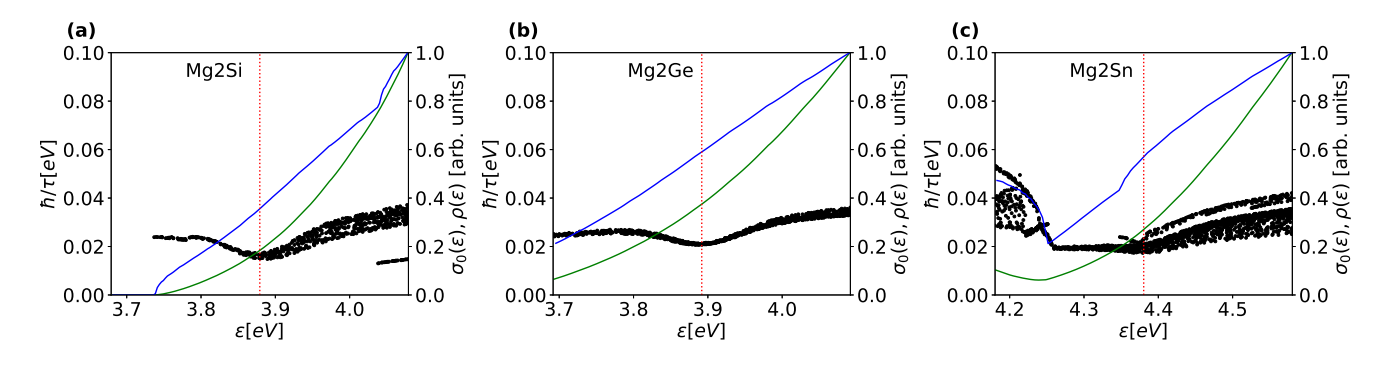


FIG. 21. Reciprocal lifetimes, \hbar/τ , at 300 K, as function of the band energies, are shown as black dots for (a) Mg₂Si, (b) Mg₂Ge and (c) Mg₂Sn . The PBEsol exchange correlation functional is used. The transport function at constant relaxation time, $\sigma_0(\epsilon)$ is shown in green, the density of states, $\rho(\epsilon)$, in blue. Arbitrary units are used. The chemical potential μ is shown using a vertical red dotted line.

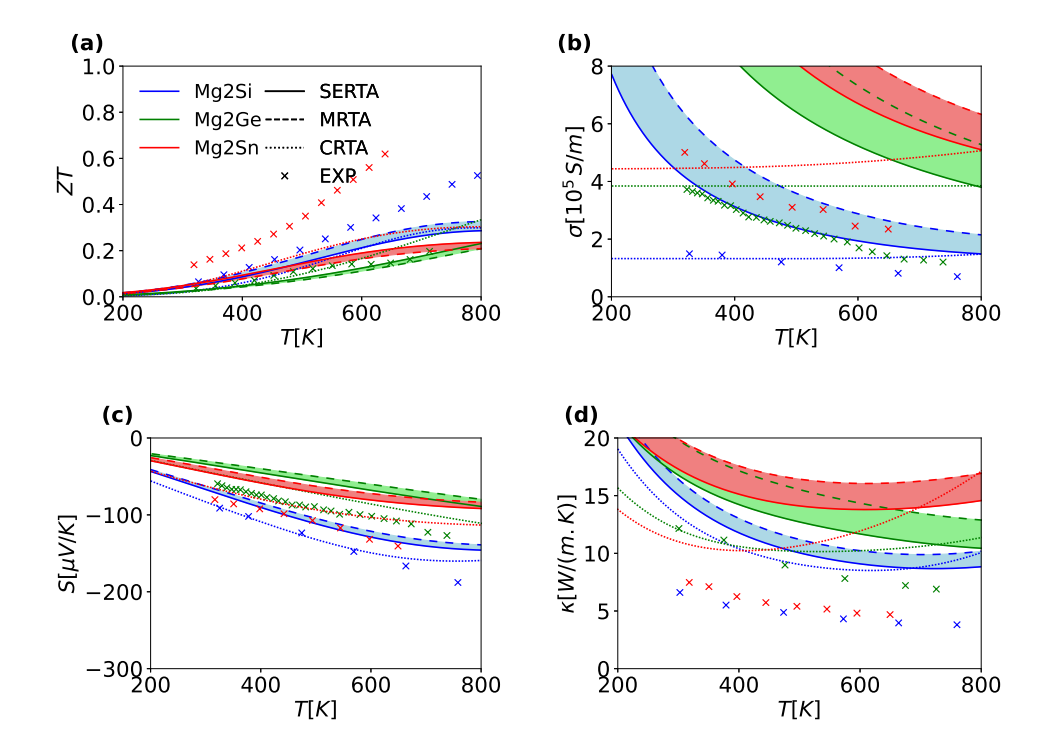


FIG. 22. Transport properties of Mg₂Si, Mg₂Ge and Mg₂S compounds computed with PBEsol. (a) ZT thermoelectric figure of merit, (b) electronic conductivity σ , (c) thermopower S, and (d) thermal conductivity κ . A k=60 mesh sampling is used. Experimental measurements^{50–52} are shown using crosses. The results of computations are shown using continuous, dashed and dotted lines for the SERTA, MRTA and CRTA approximations, respectively. For the CRTA, $\tau=10^{-14}$ s is used. To compute the lattice thermal conductivity, a sampling of q=27, q=27 and q=26 are used for Mg₂Si, Mg₂Ge and Mg₂Sn respectively. For each compound, the differences between SERTA and MRTA approximations are shown using shaded areas.

Appendix B: ERTA and MRTA

Assuming the phonon system to be at equilibrium, the collision integral, Eq. 8, can be written

$$\frac{\partial f_{\mathbf{k}n}}{\partial t}\Big|_{col} = \sum_{\mathbf{k}'n'} \left(\frac{(1 - f_{\mathbf{k}n}) f_{\mathbf{k}'n'}}{(1 - f_{\mathbf{k}n}^0) f_{\mathbf{k}'n'}^0} - \frac{f_{\mathbf{k}n}(1 - f_{\mathbf{k}'n'})}{f_{\mathbf{k}n}^0 (1 - f_{\mathbf{k}'n}^0)} \right) (1 - f_{\mathbf{k}n}^0) f_{\mathbf{k}'n'}^0
\times \frac{2\pi}{\hbar} \sum_{\mathbf{q}j} |g(\mathbf{k}n, \mathbf{k}'n', \mathbf{q}j)|^2 \left(n_{\mathbf{q}j}^0 \delta(\epsilon_{\mathbf{k}n} - \epsilon_{\mathbf{k}'n'} - \hbar\omega_{\mathbf{q}j}) + (1 + n_{-\mathbf{q}j}^0) \delta(\epsilon_{\mathbf{k}n} - \epsilon_{\mathbf{k}'n'} + \hbar\omega_{-\mathbf{q}j}) \right)$$

$$= \sum_{\mathbf{k}', \mathbf{k}'} \left(\frac{(1 - f_{\mathbf{k}n}) f_{\mathbf{k}'n'}}{(1 - f_{\mathbf{k}'n}^0) f_{\mathbf{k}'n'}^0} - \frac{f_{\mathbf{k}n}(1 - f_{\mathbf{k}'n'})}{f_{\mathbf{k}n}^0 (1 - f_{\mathbf{k}'n'}^0)} \right) (1 - f_{\mathbf{k}n}^0) f_{\mathbf{k}'n'}^0 S(\mathbf{k}'n', \mathbf{k}n).$$
(B2)

It is linearized as

$$\frac{\partial f_{\mathbf{k}n}}{\partial t}\Big|_{lin} = \sum_{\mathbf{k}'n'} \left(\frac{1 - f_{\mathbf{k}n}^0}{1 - f_{\mathbf{k}'n'}^0} \delta f_{\mathbf{k}'n'} - \frac{f_{\mathbf{k}'n'}^0}{f_{\mathbf{k}n}^0} \delta f_{\mathbf{k}n} \right) S(\mathbf{k}'n', \mathbf{k}n).$$
(B3)

If a relaxation time is defined by the relation

$$\left. \frac{\partial f_{\mathbf{k}n}}{\partial t} \right|_{lin} = -\frac{\delta f_{\mathbf{k}n}}{\tau_{\mathbf{k}n}},$$

then, using $\left(-\frac{\partial f_{\mathbf{k}n}^0}{\partial \epsilon_{\mathbf{k}n}}\right) = \frac{1}{k_B T} f_{\mathbf{k}n}^0 (1 - f_{\mathbf{k}n}^0)$, the Boltzmann equation can be rewritten as an equation for $\tau_{\mathbf{k}n}$,

$$\frac{1}{\tau_{\mathbf{k}n}} = \sum_{\mathbf{k}'n'} \frac{f_{\mathbf{k}'n'}^{0}}{f_{\mathbf{k}n}^{0}} \left(1 - \frac{\tau_{\mathbf{k}'n'} \mathbf{G}_{\mathbf{k}'n'} \cdot \mathbf{v}_{\mathbf{k}'n'}}{\tau_{\mathbf{k}n} \mathbf{G}_{\mathbf{k}n} \cdot \mathbf{v}_{\mathbf{k}n}} \right) S(\mathbf{k}'n', \mathbf{k}n)$$
(B4)

where we have defined the vector of applied fields,

$$\mathbf{G}_{\mathbf{k}n} = (\epsilon_{\mathbf{k}n} - \mu) \frac{\nabla T}{T} + e\mathbf{\mathcal{E}}.$$
 (B5)

The above equation means that the relaxation time depends on the applied fields. Two different approximations are obtained when we assume the $G_{\mathbf{k}n}$ vector to be a pure electric field or a pure temperature gradient.

We have to consider those two cases because then the dot product in Eq. B4 can be performed along a vector independent of the wavevector. Therefore in Eq. B4, the group velocities of the states $\mathbf{k}n$ and $\mathbf{k}'n'$ are projected in the same direction. Denoting this vector \mathbf{G} , this allows to use the law of cosines to write⁷³

$$\cos\left(\mathbf{G}, \mathbf{v}_{\mathbf{k}'n'}\right) = \cos\left(\mathbf{v}_{\mathbf{k}n}, \mathbf{v}_{\mathbf{k}'n'}\right) \cos\left(\mathbf{G}, \mathbf{v}_{\mathbf{k}n}\right) + \sin\left(\mathbf{v}_{\mathbf{k}n}, \mathbf{v}_{\mathbf{k}'n'}\right) \sin\left(\mathbf{G}, \mathbf{v}_{\mathbf{k}n}\right) \cos\phi'$$
(B6)

where ϕ' is the angle between the planes $\mathbf{v}_{\mathbf{k}n}$, $\mathbf{v}_{\mathbf{k}'n'}$ and \mathbf{G} , $\mathbf{v}_{\mathbf{k}n}$. If nothing would depend on ϕ' in the integrand of Eq. B4, $\cos \phi'$ would average to zero in the integration over \mathbf{k}' , in which case we could use

$$\frac{\cos\left(\mathbf{G}, \mathbf{v}_{\mathbf{k}'n'}\right)}{\cos\left(\mathbf{G}, \mathbf{v}_{\mathbf{k}n}\right)} = \cos\left(\mathbf{v}_{\mathbf{k}n}, \mathbf{v}_{\mathbf{k}'n'}\right) = \frac{\mathbf{v}_{\mathbf{k}n} \cdot \mathbf{v}_{\mathbf{k}'n'}}{|\mathbf{v}_{\mathbf{k}n}| |\mathbf{v}_{\mathbf{k}'n'}|}$$
(B7)

and

$$\frac{1}{\tau_{\mathbf{k}n}} = \sum_{\mathbf{k'}n'} \frac{f_{\mathbf{k'}n'}^0}{f_{\mathbf{k}n}^0} \left(1 - \frac{\tau_{\mathbf{k'}n'} |\mathbf{v}_{\mathbf{k'}n'}|}{\tau_{\mathbf{k}n} |\mathbf{v}_{\mathbf{k}n}|} \frac{\mathbf{G}_{\mathbf{k'}n'} \cdot \mathbf{G}}{\mathbf{G}_{\mathbf{k}n} \cdot \mathbf{G}} \frac{\mathbf{v}_{\mathbf{k}n} \cdot \mathbf{v}_{\mathbf{k'}n'}}{|\mathbf{v}_{\mathbf{k}n}| |\mathbf{v}_{\mathbf{k'}n'}|} \right) S(\mathbf{k'}n', \mathbf{k}n).$$
(B8)

To eliminate the relaxation time from the right hand side, one further assumption has to be made. Often in the literature²⁸ it is assumed that $\tau_{\mathbf{k}'n'} \approx \tau_{\mathbf{k}n}$ and we get

$$\frac{1}{\tau_{\mathbf{k}n}} = \sum_{\mathbf{k}'n'} \frac{f_{\mathbf{k}'n'}^0}{f_{\mathbf{k}n}^0} \left(1 - \frac{\mathbf{G}_{\mathbf{k}'n'} \cdot \mathbf{G}}{\mathbf{G}_{\mathbf{k}n} \cdot \mathbf{G}} \frac{\mathbf{v}_{\mathbf{k}n} \cdot \mathbf{v}_{\mathbf{k}'n'}}{|\mathbf{v}_{\mathbf{k}n}|^2} \right) S(\mathbf{k}'n', \mathbf{k}n).$$
(B9)

However, with this approximation the relaxation could become negative²⁸. Therefore, instead of assuming the relaxation to be a weak function of \mathbf{k} , we assume that the mean free path is such a weak function of \mathbf{k} , $\tau_{\mathbf{k}'n'}|\mathbf{v}_{\mathbf{k}'n'}| \approx \tau_{\mathbf{k}n}|\mathbf{v}_{\mathbf{k}n}|$. Then we get

$$\frac{1}{\tau_{\mathbf{k}n}} = \sum_{\mathbf{k}'n'} \frac{f_{\mathbf{k}'n'}^0}{f_{\mathbf{k}n}^0} \left(1 - \frac{\mathbf{G}_{\mathbf{k}'n'} \cdot \mathbf{G}}{\mathbf{G}_{\mathbf{k}n} \cdot \mathbf{G}} \frac{\mathbf{v}_{\mathbf{k}n} \cdot \mathbf{v}_{\mathbf{k}'n'}}{|\mathbf{v}_{\mathbf{k}n}| |\mathbf{v}_{\mathbf{k}'n'}|} \right) S(\mathbf{k}'n', \mathbf{k}n).$$
(B10)

For pure electric field, $G_{kn} = e\mathcal{E}$, and $G = \mathcal{E}$, this gives the momentum relaxation time approximation (MRTA)

$$\frac{1}{\tau_{\mathbf{k}n}^{\text{MRTA}}} = \sum_{\mathbf{k}'n'} \frac{f_{\mathbf{k}'n'}^{0}}{f_{\mathbf{k}n}^{0}} \left(1 - \frac{\mathbf{v}_{\mathbf{k}n} \cdot \mathbf{v}_{\mathbf{k}'n'}}{|\mathbf{v}_{\mathbf{k}n}||\mathbf{v}_{\mathbf{k}'n'}|}\right) S(\mathbf{k}'n', \mathbf{k}n) \tag{B11}$$

$$= \frac{2\pi}{\hbar} \sum_{\mathbf{k}'n'} \sum_{\mathbf{q}j} |g(\mathbf{k}n, \mathbf{k}'n', \mathbf{q}j)|^{2} \frac{f_{\mathbf{k}'n'}^{0}}{f_{\mathbf{k}n}^{0}} \left(n_{\mathbf{q}j}^{0} \delta(\epsilon_{\mathbf{k}n} - \epsilon_{\mathbf{k}'n'} - \hbar\omega_{\mathbf{q}j}) + (1 + n_{-\mathbf{q}j}^{0}) \delta(\epsilon_{\mathbf{k}n} - \epsilon_{\mathbf{k}'n'} + \hbar\omega_{-\mathbf{q}j})\right)$$

$$\times \left(1 - \frac{\mathbf{v}_{\mathbf{k}n} \cdot \mathbf{v}_{\mathbf{k}'n'}}{|\mathbf{v}_{\mathbf{k}n}||\mathbf{v}_{\mathbf{k}'n'}|}\right)$$

$$= \frac{2\pi}{\hbar} \sum_{\mathbf{k}'n'} \sum_{\mathbf{q}j} |g(\mathbf{k}n, \mathbf{k}'n', \mathbf{q}j)|^{2} \left((1 + n_{\mathbf{q}j}^{0} - f_{\mathbf{k}'n'}^{0}) \delta(\epsilon_{\mathbf{k}n} - \epsilon_{\mathbf{k}'n'} - \hbar\omega_{\mathbf{q}j}) + (f_{\mathbf{k}'n'}^{0} + n_{-\mathbf{q}j}^{0}) \delta(\epsilon_{\mathbf{k}n} - \epsilon_{\mathbf{k}'n'} + \hbar\omega_{-\mathbf{q}j})\right)$$

$$\times \left(1 - \frac{\mathbf{v}_{\mathbf{k}n} \cdot \mathbf{v}_{\mathbf{k}'n'}}{|\mathbf{v}_{\mathbf{k}n}||\mathbf{v}_{\mathbf{k}'n'}|}\right)$$
(B13)

Therefore the computation of the momentum relaxation time is the same than for the SERTA approximation, except for the last factor which gives more weight to back scattering events.

For pure thermal gradient, $\mathbf{G}_{\mathbf{k}n} = (\epsilon_{\mathbf{k}n} - \mu) \frac{\nabla T}{T}$, and $\mathbf{G} = \nabla T$, this gives the energy relaxation time approximation (ERTA),

$$\frac{1}{\tau_{\mathbf{k}n}^{\text{ERTA}}} = \sum_{\mathbf{k}'n'} \frac{f_{\mathbf{k}'n'}^{0}}{f_{\mathbf{k}n}^{0}} \left(1 - \frac{\epsilon_{\mathbf{k}'n'} - \mu}{\epsilon_{\mathbf{k}n} - \mu} \frac{\mathbf{v}_{\mathbf{k}n} \cdot \mathbf{v}_{\mathbf{k}'n'}}{|\mathbf{v}_{\mathbf{k}n}||\mathbf{v}_{\mathbf{k}'n'}|} \right) S(\mathbf{k}'n', \mathbf{k}n)$$

$$= \frac{2\pi}{\hbar} \sum_{\mathbf{k}'n'} \sum_{\mathbf{q}j} |g(\mathbf{k}n, \mathbf{k}'n', \mathbf{q}j)|^{2} \left((1 + n_{\mathbf{q}j}^{0} - f_{\mathbf{k}'n'}^{0}) \delta(\epsilon_{\mathbf{k}n} - \epsilon_{\mathbf{k}'n'} - \hbar\omega_{\mathbf{q}j}) + (f_{\mathbf{k}'n'}^{0} + n_{-\mathbf{q}j}^{0}) \delta(\epsilon_{\mathbf{k}n} - \epsilon_{\mathbf{k}'n'} + \hbar\omega_{-\mathbf{q}j}) \right)$$

$$\times \left(1 - \frac{\epsilon_{\mathbf{k}'n'} - \mu}{\epsilon_{\mathbf{k}'n} - \mu} \frac{\mathbf{v}_{\mathbf{k}n} \cdot \mathbf{v}_{\mathbf{k}'n'}}{|\mathbf{v}_{\mathbf{k}n}||\mathbf{v}_{\mathbf{k}'n'}|} \right).$$
(B15)

Appendix C: Gauss-Legendre integration

In the integral Eq. 23, we can make the substitution $x = 1 - 2f^0$. $x(\epsilon)$ is a monotonic function, going from -1 to 1 as ϵ goes from $-\infty$ to ∞ . Moreover, $x(\mu) = 0$. Using $dx = 2\frac{\partial f}{\partial \mu}d\epsilon$ and $\epsilon = \mu + k_BT \ln \frac{1+x}{1-x}$, we obtain

$$\mathcal{L}_{ij} = \frac{1}{2} \left(\frac{k_B T}{-e} \right)^{i+j-2} \int_{-1}^{+1} dx \left(\ln \frac{1+x}{1-x} \right)^{i+j-2} \sigma(\mu + k_B T \ln \frac{1+x}{1-x}). \tag{C1}$$

The transport function $\sigma(\epsilon)$ is assumed to be zero outside the interval $(\epsilon_{\min}, \epsilon_{\max})$, therefore the integrand of the above interval is assumed to be zero outside $(x(\epsilon_{\min}), x(\epsilon_{\max}))$. This way x is never reaching -1 or +1 and therefore $\ln \frac{1+x}{1-x}$ is never becoming infinite. Under those conditions, the above integral can be approximated using the Gauss-Legendre quadrature

$$\mathcal{L}_{ij} \approx \frac{1}{2} \left(\frac{k_B T}{-e} \right)^{i+j-2} \sum_{k=1}^{N} \left(\ln \frac{1+x_k}{1-x_k} \right)^{i+j-2} \sigma(\mu + k_B T \ln \frac{1+x_k}{1-x_k}) w_k, \tag{C2}$$

where x_k are the roots of the Legendre polynomial of order N, $P_N(x)$, and the weight w_k are

$$w_k = \frac{2(1 - x_k^2)}{[(N+1)P_{N+1}(x_k)]^2},\tag{C3}$$

with $P_0(x) = 1$, $P_1(x) = x$, $P_2(x) = 1/2(3x^2 - 1)$, and $P_n(x) = (2n - 1)/nxP_{n-1}(x) - (n - 2)/nP_{n-2}(x)$ for n > 2. This integration method is valuable for the calculation of transport properties. Indeed, the integrand is approximated by an Hermite interpolating polynomial. It means that the interpolating polynomial matches the values of the integrand at the points x_k , but also matches the values of its derivative. This provides an increased smoothness for the interpolation. Finally, the Gauss-Legendre method is obtained by choosing the x_k such that the part of the interpolation involving the derivatives of the function to be integrated does not contribute to the integral. This choice ensures that the quadrature can take the form $\sum_k f(x_k)w_k$ rather than $\sum_k f(x_k)w_k + f'(x_k)u_k$, which would be inconvenient in our case since the derivative of the transport function is not known. Finally, the x_k being the roots of the Legendre polynomials guarantees they are symmetric around x = 0 (the chemical potential), and that the weights are maximum around that point.

Appendix D: Electron's velocities

The expectation value of the velocity operator is obtained from the derivative of the band structure,

$$\mathbf{v}_{\mathbf{k}n} = \langle \varphi_{\mathbf{k}n} | \mathbf{v} | \varphi_{\mathbf{k}n} \rangle = \langle \varphi_{\mathbf{k}n} | \frac{i}{\hbar} [H, \mathbf{r}] | \varphi_{\mathbf{k}n} \rangle = \frac{1}{\hbar} \frac{\partial \epsilon_{\mathbf{k}n}}{\partial \mathbf{k}}. \tag{D1}$$

This relation is valid for a general one particle Hamiltonian H, even if including spin orbit coupling or a Hubbard U correction.

We would like to perform the above derivative with respect to \mathbf{k} within the framework of the PAW method⁷⁴. To do this, we proceed along the line which is used in the Heisenberg representation to take time derivative. We define \mathbf{k} dependent operators as

$$A_{\mathbf{k}} = e^{-i\mathbf{k}\cdot\mathbf{r}} A e^{i\mathbf{k}\cdot\mathbf{r}} \tag{D2}$$

and obtain their derivative,

$$\frac{\partial A_{\mathbf{k}}}{\partial \mathbf{k}} = i[A_{\mathbf{k}}, \mathbf{r}] + e^{-i\mathbf{k}\cdot\mathbf{r}} \frac{\partial A}{\partial \mathbf{k}} e^{i\mathbf{k}\cdot\mathbf{r}}.$$
 (D3)

The second term is zero if the operator does not have an intrinsic k dependence.

In the PAW method, we have the equations

$$\tilde{h}|\tilde{\varphi}_{\mathbf{k}n}\rangle = \epsilon_{\mathbf{k}n}\tilde{o}|\tilde{\varphi}_{\mathbf{k}n}\rangle \tag{D4}$$

$$\langle \tilde{\varphi}_{\mathbf{k}n} | \tilde{o} | \tilde{\varphi}_{\mathbf{k}n'} \rangle = \delta_{nn'} \tag{D5}$$

$$\tilde{h} = -\frac{\hbar^2}{2m} \nabla^2 + v_l + \sum_{l\tau} \sum_{LL'} |\tilde{p}_L(l\tau)\rangle D_{LL'}(l\tau) \langle \tilde{p}_{L'}(l\tau)|$$
(D6)

$$\tilde{o} = 1 + \sum_{l\tau} \sum_{LL'} |\tilde{p}_L(l\tau)\rangle Q_{LL'}(l\tau)\langle \tilde{p}_{L'}(l\tau)|$$
(D7)

where l and τ label the lattice vectors and the atoms in a primitive unit cell, and L and L' quantum numbers used to label atomic orbitals.

Using the periodic part of the Bloch wavefunctions, $\tilde{u}_{\mathbf{k}n}$,

$$\tilde{\varphi}_{\mathbf{k}n}(\mathbf{r}) = e^{i\mathbf{k}\cdot\mathbf{r}}\tilde{u}_{\mathbf{k}n}(\mathbf{r}),\tag{D8}$$

the above equations become

$$\tilde{h}_{\mathbf{k}}|\tilde{u}_{\mathbf{k}n}\rangle = \epsilon_{\mathbf{k}n}\tilde{o}_{\mathbf{k}}|\tilde{u}_{\mathbf{k}n}\rangle$$
 (D9)

$$\langle \tilde{u}_{\mathbf{k}n} | \tilde{o}_{\mathbf{k}} | \tilde{u}_{\mathbf{k}n'} \rangle = \delta_{nn'}$$
 (D10)

$$\tilde{h}_{\mathbf{k}} = e^{-i\mathbf{k}\cdot\mathbf{r}}\tilde{h}e^{i\mathbf{k}\cdot\mathbf{r}} = -\frac{\hbar^2}{2m}(\nabla + i\mathbf{k})^2 + v_l + \sum_{l,\tau}\sum_{LL'}e^{-i\mathbf{k}\cdot\mathbf{r}}|\tilde{p}_L(l\tau)\rangle D_{LL'}(l\tau)\langle\tilde{p}_{L'}(l\tau)|e^{i\mathbf{k}\cdot\mathbf{r}}$$
(D11)

$$\tilde{o}_{\mathbf{k}} = e^{-i\mathbf{k}\cdot\mathbf{r}}\tilde{o}e^{i\mathbf{k}\cdot\mathbf{r}} = 1 + \sum_{l\tau} \sum_{LL'} e^{-i\mathbf{k}\cdot\mathbf{r}} |\tilde{p}_L(l\tau)\rangle Q_{LL'}(l\tau)\langle \tilde{p}_{L'}(l\tau)|e^{i\mathbf{k}\cdot\mathbf{r}}$$
(D12)

Eq. D9 gives

$$\langle \tilde{u}_{\mathbf{k}n} | \tilde{h}_{\mathbf{k}} | \tilde{u}_{\mathbf{k}n} \rangle = \epsilon_{\mathbf{k}n} \langle \tilde{u}_{\mathbf{k}n} | \tilde{o}_{\mathbf{k}} | \tilde{u}_{\mathbf{k}n} \rangle.$$
 (D13)

As a standard result of perturbation theory, the first order change of the eigenvalues can be obtained differentiating the above equation, and using Eqs. D9 and D10. We obtain

$$\frac{\partial \epsilon_{\mathbf{k}n}}{\partial \mathbf{k}} = \langle \tilde{u}_{\mathbf{k}n} | \frac{\partial \tilde{h}_{\mathbf{k}}}{\partial \mathbf{k}} - \epsilon_{\mathbf{k}n} \frac{\partial \tilde{o}_{\mathbf{k}}}{\partial \mathbf{k}} | \tilde{u}_{\mathbf{k}n} \rangle. \tag{D14}$$

The derivatives with respect to \mathbf{k} in the above equation are now computed from the commutator with the position operator, as in Eq. D3, assuming the Hamiltonian and overlap operators does not have an intrinsic \mathbf{k} dependence.

$$\frac{\partial \epsilon_{\mathbf{k}n}}{\partial \mathbf{k}} = i \langle \tilde{u}_{\mathbf{k}n} | [\tilde{h}_{\mathbf{k}}, \mathbf{r}] - \epsilon_{\mathbf{k}n} [\tilde{o}_{\mathbf{k}}, \mathbf{r}] | \tilde{u}_{\mathbf{k}n} \rangle \tag{D15}$$

$$= \langle \tilde{u}_{\mathbf{k}n} | \frac{\hbar}{m} (-i\hbar \nabla + \hbar \mathbf{k}) | \tilde{u}_{\mathbf{k}n} \rangle \tag{D16}$$

$$+ i \sum_{l\tau} \sum_{LL'} \langle \tilde{u}_{\mathbf{k}n} | \left[e^{-i\mathbf{k}\cdot\mathbf{r}} | \tilde{p}_{L}(l\tau) \rangle (D_{LL'}(l\tau) - \epsilon_{\mathbf{k}n} Q_{LL'}(l\tau)) \langle \tilde{p}_{L'}(l\tau) | e^{i\mathbf{k}\cdot\mathbf{r}}, \mathbf{r} \right] | \tilde{u}_{\mathbf{k}n} \rangle \tag{D16}$$

$$= \langle \tilde{u}_{\mathbf{k}n} | \frac{\hbar}{m} (-i\hbar \nabla + \hbar \mathbf{k}) | \tilde{u}_{\mathbf{k}n} \rangle
+ i \sum_{l\tau} \sum_{LL'} \langle \tilde{u}_{\mathbf{k}n} | \left[e^{-i\mathbf{k}\cdot(\mathbf{r}-\mathbf{R}_{l\tau})} | \tilde{p}_{L}(l\tau) \rangle (D_{LL'}(l\tau) - \epsilon_{\mathbf{k}n} Q_{LL'}(l\tau)) \langle \tilde{p}_{L'}(l\tau) | e^{i\mathbf{k}\cdot(\mathbf{r}-\mathbf{R}_{l\tau})}, \mathbf{r} - \mathbf{R}_{l\tau} \right] | \tilde{u}_{\mathbf{k}n} \rangle \tag{D17}$$

Using Bloch wavefunctions the final results can also be written as

$$\frac{\partial \epsilon_{\mathbf{k}n}}{\partial \mathbf{k}} = \frac{1}{m} \langle \tilde{\varphi}_{\mathbf{k}n} | -i\hbar \nabla | \tilde{\varphi}_{\mathbf{k}n} \rangle + i \sum_{l\tau} \sum_{LL'} (D_{LL'}(l\tau) - \epsilon_{\mathbf{k}n} Q_{LL'}(l\tau))
\times \left[\langle \tilde{\varphi}_{\mathbf{k}n} | \tilde{p}_L(l\tau) \rangle \langle \tilde{p}_{L'}(l\tau) | \mathbf{r} - \mathbf{R}_{l\tau} | \tilde{\varphi}_{\mathbf{k}n} \rangle - \langle \tilde{\varphi}_{\mathbf{k}n} | \mathbf{r} - \mathbf{R}_{l\tau} | \tilde{p}_L(l\tau) \rangle \langle \tilde{p}_{L'}(l\tau) | | \tilde{\varphi}_{\mathbf{k}n} \rangle \right].$$
(D18)

V. EXAMPLE CASE: SI

In this appendix we consider cubic silicon. The ab initio calculations were performed using a cut off energy of 400 eV and for transport calculations Brillouin zone integrals are performed using a $100 \times 100 \times 100$ uniform grid. Because we consider low carrier concentration, the energy integrals of the Onsager coefficients are performed using 5001 points.

The electron and hole mobilities are defined as the ratio between the band-resolved electrical conductivity and the corresponding carrier density,

$$\mu_{ep}^e = \frac{\sigma_{n \in CB}}{n_e}, \quad n_e = \frac{1}{V_0 N} \sum_{\mathbf{k}n \in CB} f^0(\varepsilon_{\mathbf{k}n}, T, \mu), \quad (1)$$

$$\mu_{ep}^{h} = \frac{\sigma_{n \in VB}}{n_h}, \quad n_h = \frac{1}{V_0 N} \sum_{\mathbf{k}n \in VB} [1 - f^0(\varepsilon_{\mathbf{k}n}, T, \mu)],$$
(2)

where $\sigma_{n \in CB}$ and $\sigma_{n \in VB}$ are the conductivites from conduction-band (CB) and valence-band (VB) states.

The mobility of n-type silicon, computed using the MRTA approximation, at 300 K, is shown as a function of the impurity donors concentration in Fig. 23. Black lines are used to show the results using the PBE, PBEsol, and LDA exchange correlation functionals. Experimental measurements from 75, similar to those used in⁶⁶, are shown using black dots. We observe that above $n \approx 10^{16} \, \mathrm{cm}^{-3}$, the difference between calculations and experiments becomes significant. The calculated electron-phonon-limited mobilities ($\mu_{\rm ep}$) for silicon at 300 K are 1388 (PBE), 1489 (PBEsol), and 1534 (LDA) cm² V⁻¹ s⁻¹, in good agreement with previous theoretical results. Indeed, although the details of the electronic structure calculations and Boltzmann equation solvers may differ, previous works report mobilities of 1343 and $1296 \,\mathrm{cm}^2/(\mathrm{V} \cdot \mathrm{s})$ for PBE^{66,76}, and 1509, 1555, 1385, and $1970 \,\mathrm{cm^2/(V \cdot s)}$ for LDA^{18,66,67,77}.

Most of the discrepancy between theory and experiment comes from the neglect of impurity scattering. In⁶⁶ the formula derived by Debye and Conwell⁶⁵, under the assumptions of free electrons and power scattering laws for phonons and impurities, was used to take into account the effect of impurity scattering. The above mentioned formula may be written as

$$\mu = \mu_{ep} \Big(1 + X^2 [\operatorname{ci}(X) \cos(X) + \operatorname{si}(X) \sin(X)] \Big),$$
 (3)

with $X = \sqrt{6\mu_{ep}/\mu_{ei}}$, μ_{ei} the mobility due to electronimpurity scattering and μ_{ep} the mobility due to electronphonon scattering which is computed in the present work. For n-type silicon, Li et al. 78 proposed the empirical formula

$$\mu_{ei} = \frac{7.3 \times 10^{17} \, T^{3/2}}{nG(b)},\tag{4}$$

with
$$G(b) = \ln(b + 1) - b/(b + 1)$$
, $b = 24\epsilon m^*(k_BT)^2/(\hbar^2e^2n)$, $\epsilon = 11.9\epsilon_0$ and $m^* = 1.08m$.

When it is used in Eq. 3, we obtain the gray curves in Fig. 23 which reconcile theory and experiment.

The effect of impurity scattering is also clearly visible with temperature. In Fig. 24 the mobility is plotted as a function of temperature, as a dark blue curve for low doping concentration $(n=2.75\times 10^{14}\,\mathrm{cm^{-3}})$, and as a dark green curve for higher doping $(n=2\times 10^{19}\,\mathrm{cm^{-3}})$. The same experimental values than in 67 are used. The data shown as blue dots, for low concentrations, are taken from 79 . For higher concentration, the data shown as green dots, diamonds and stars are taken from 80 . For low doping concentration the agreement with experiments is excellent, but at higher doping the effect of impurities needs to be considered. Eq. 3 is used to obtain the light blue and green curves, denoted as PBE+I. Once again this empirical formula yields better agreement with experiment.

The result of this section evidences that for highly doped compounds, the effect of impurities cannot be neglected. In the case of silicon, such an effect can be described using a simple model, as long as an empirical formula like Eq. 4 is available.

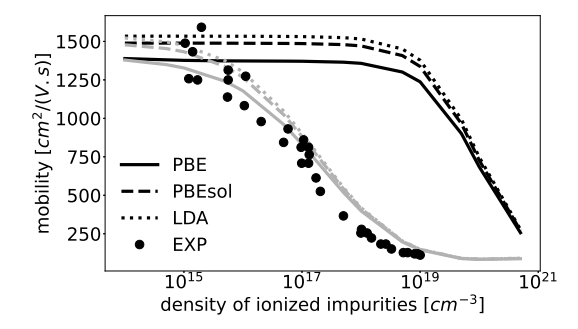


FIG. 23. Mobility of silicon as a function of the impurity donors concentration at 300 K. The lines show the results obtained for the PBE, PBEsol and LDA exchange correlation functionals, while the gray lines correspond to the same calculations but accounting for impurity scattering according to the Debye and Conwell⁶⁵ formula.

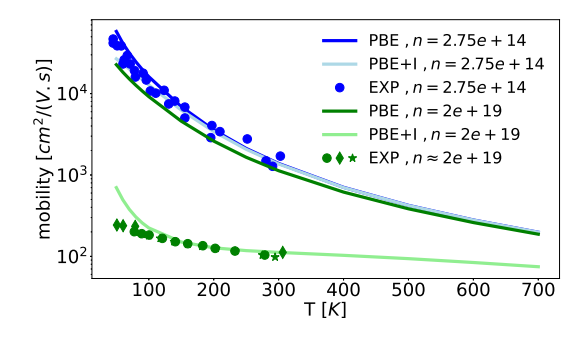


FIG. 24. Mobility of silicon as a function of temperature for different carrier concentration. Dark blue and green lines show the results obtained for $n=2.75\times 10^{14} {\rm cm}^{-3}$ and $n=2\times 10^{19} {\rm cm}^{-3}$ respectively. The light blue and green lines correspond to the same calculations but accounting for impurity scattering according to the Debye and Conwell⁶⁵ formula

VI. SPIN ORBIT COUPLING

In this appendix we discuss the effect of spin-orbit coupling on electrical conductivity for Si and PbSe.

 ${\rm In}^{66}$ it is shown that SOC is important for p-type silicon. Using the experimental lattice parameter, we obtain, in the SERTA approximation, 586 (PBE) and 638 (PBE+SOC) in good agreement with the results obtained in ${\rm ^{81}}$ 574 and ${\rm 611cm^2/(V.s)}$ from an iterative solution of the Boltzmann equation. The experimental value is ${\rm 502cm^2/(V.s)}$, which can only be obtained when additional corrections are applied (see ${\rm ^{66}}$). This example reinforces our previous comment about SOC, it is not always beneficial at the level of semi-local functionals.

The results we obtain for PbSe are shown in Fig. 27. It can be seen that including spin-orbit coupling leads to better agreement with experiment for PBEsol, but not for PBE. We can understand this result as a consequence

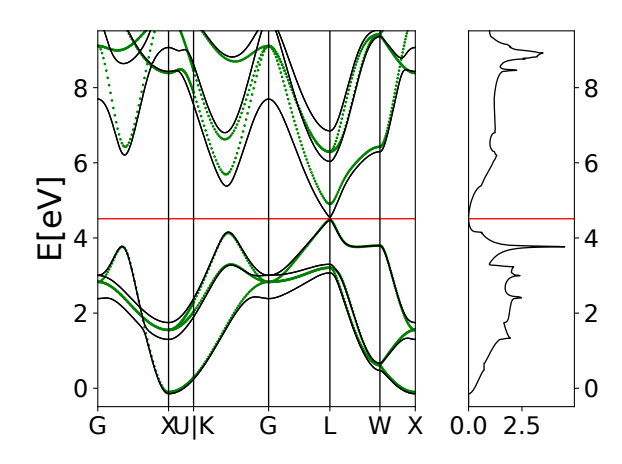


FIG. 25. Electronic structure of PbSe using the PBE exchange correlation functional, with (black) and without (green) spin orbit coupling.

of changes in the effective mass. As shown in Fig. 25, including SOC has little effect on the valance band for PBE. In constrast, Fig. 26 shows that SOC increases the effective mass when PBEsol is used, which consequently leads to a reduction in electrical conductivity, as observed in Fig. 27.

This improved agreement with experiment should, however, be interpreted with caution. The calculated effective mass is approximately 0.3 for PBEsol and 0.6 for PBEsol+SOC. The PBEsol+SOC result seems too large compared to the experimental value (0.28 at 300K in⁸²). Therefore the better agreement we obtain with PBEsol+SOC on the conductivity may only be accidental. When impurity scattering is considered in Fig. 27, it is no longer obvious that the agreement with experiment is better for PBEsol+SOC+I, PBE+I may already be sufficient.

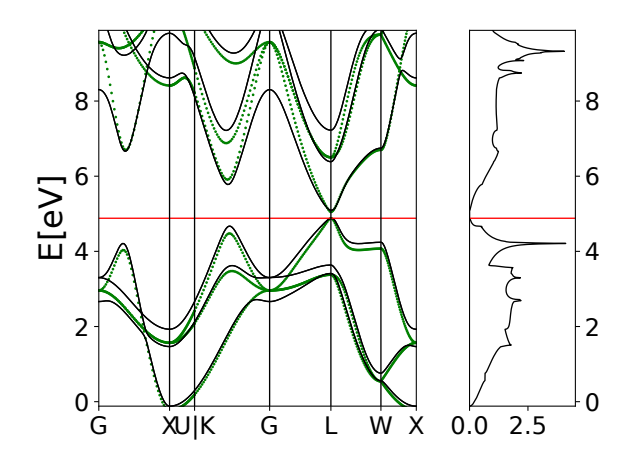
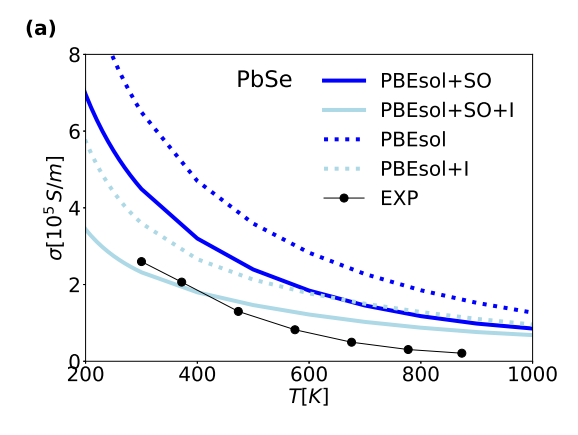


FIG. 26. Electronic structure of PbSe using the PBEsol exchange correlation functional, with (black) and without (green) spin orbit coupling.



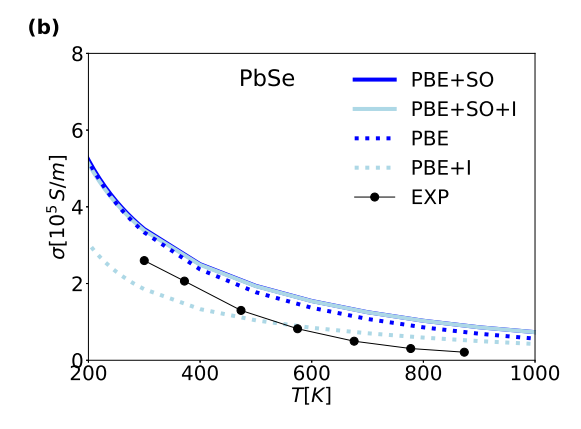


FIG. 27. Electrical conductivity of PbSe computed with the PBEsol (a) and PBE (b) exchange correlation functionals. +SO in the legend means that spin-orbit coupling is included. +I in the legend means that impurity scattering has been considered using the Debye and Conwell⁶⁵ formula with the Brooks-Herring model, as explained in the main text. Details about the experimental values are given in Tab. II

 * laurent.chaput@univ-lorraine.fr

Philip L. Taylor and Olle Heinonen. A Quantum Approach to Condensed Matter Physics. Cambridge University Press, 2002.

² John F Nye. Physical Properties of Crystals: Their Representation by Tensors and Matrices. Oxford University Press, United Kingdom, 1957.

³ S. R. De Groot and P Mazur. <u>Non equilibrium</u> thermodynamics. Dover, New York, 1984.

⁴ Qichen Song, Te-Huan Liu, Jiawei Zhou, Zhiwei Ding, and Gang Chen. Ab initio study of electron mean free paths and thermoelectric properties of lead telluride. <u>Materials</u> Today Physics, 2:69–77, 2017.

⁵ Ao Wu, Yujie Xia, Yiming Zhang, Lei Peng, Hezhu Shao, Yan Cen, Heyuan Zhu, and Hao Zhang. Strong electron-phonon and phonon-phonon interactions lead to high thermoelectric performances in lead phosphorene via symmetry breaking. Advanced Theory and Simulations, 6(12):2300226, 2023.

⁶ Jinlong Ma, Yani Chen, Wu Li, and Xiaobing Luo. Predictability of thermoelectric figure of merit for the single crystal from first principles. <u>International Journal of Heat</u> and Mass Transfer, 221:125063, 2024.

Antonio Cappai, Claudio Melis, and Luciano Colombo. Role of electron-phonon scattering on thermoelectric coefficients in pristine cs₂naybcl₆ perovskite: A full dft approach. Phys. Rev. Mater., 9:054605, May 2025.

⁸ Jeet Kumar Brahma, Farrukh Khalid, and Pankaj Kalita. Computational insights to electron-phonon and phonon-phonon interactions in agx (x = br, cl): Refining thermoelectric property predictions. <u>Journal of Physics and Chemistry of Solids</u>, 200:112620, 2025.

⁹ C. Li, N.H. Protik, P. Ordejón, and D. Broido. Colossal phonon drag enhanced thermopower in lightly doped diamond. Materials Today Physics, 27:100740, 2022.

Atsushi Togo, Laurent Chaput, and Isao Tanaka. Distributions of phonon lifetimes in brillouin zones. Phys. Rev.

B, 91:094306, Mar 2015.

Wu Li, Jesús Carrete, Nebil A. Katcho, and Natalio Mingo. ShengBTE: a solver of the Boltzmann transport equation for phonons. Comp. Phys. Commun., 185:1747–1758, 2014.

Arash A. Mostofi, Jonathan R. Yates, Giovanni Pizzi, Young-Su Lee, Ivo Souza, David Vanderbilt, and Nicola Marzari. An updated version of wannier90: A tool for obtaining maximally-localised wannier functions. Computer Physics Communications, 185(8):2309–2310, 2014.

Feliciano Giustino. Electron-phonon interactions from first principles. Rev. Mod. Phys., 89:015003, Feb 2017.

S. Poncé, E.R. Margine, C. Verdi, and F. Giustino. Epw: Electron-phonon coupling, transport and superconducting properties using maximally localized wannier functions. Computer Physics Communications, 209:116–133, 2016.

Georg K.H. Madsen, Jesús Carrete, and Matthieu J. Verstraete. Boltztrap2, a program for interpolating band structures and calculating semi-classical transport coefficients. Computer Physics Communications, 231:140–145, 2018.

Nakib H. Protik, Chunhua Li, Miguel Pruneda, David Broido, and Pablo Ordejón. The elphbolt ab initio solver for the coupled electron-phonon boltzmann transport equations. npj Computational Materials, 8(1), February 2022.

Wu Li. Electrical transport limited by electron-phonon coupling from boltzmann transport equation: An ab initio study of si, al, and mos₂. Phys. Rev. B, 92:075405, Aug 2015.

¹⁸ Guillaume Brunin, Henrique Pereira Coutada Miranda, Matteo Giantomassi, Miquel Royo, Massimiliano Stengel, Matthieu J. Verstraete, Xavier Gonze, Gian-Marco Rignanese, and Geoffroy Hautier. Phonon-limited electron mobility in si, gaas, and gap with exact treatment of dynamical quadrupoles. Phys. Rev. B, 102:094308, Sep 2020.

L. Chaput, Atsushi Togo, and Isao Tanaka. Finite-displacement computation of the electron-phonon interac-

tion within the projector augmented-wave method. Phys. Rev. B, 100:174304, Nov 2019.

Manuel Engel, Henrique Miranda, Laurent Chaput, Atsushi Togo, Carla Verdi, Martijn Marsman, and Georg Kresse. Zero-point renormalization of the band gap of semiconductors and insulators using the projector augmented wave method. Phys. Rev. B, 106:094316, Sep 2022.

P. E. Blöchl. Projector augmented-wave method. Phys. Rev. B, 50:17953–17979, Dec 1994.

G. Kresse and J. Hafner. Ab initio molecular dynamics for liquid metals. Phys. Rev. B, 47:558–561, Jan 1993.

²³ G. Kresse and J. Hafner. Ab initio molecular-dynamics simulation of the liquid-metal-amorphous-semiconductor transition in germanium. <u>Phys. Rev. B</u>, 49:14251–14269, May 1994.

²⁴ G. Kresse and J. Furthmüller. Efficiency of ab-initio total energy calculations for metals and semiconductors using a plane-wave basis set. <u>Computational Materials Science</u>, 6(1):15–50, 1996.

²⁵ G. Kresse and J. Furthmüller. Efficient iterative schemes for ab initio total-energy calculations using a plane-wave basis set. Phys. Rev. B, 54:11169–11186, Oct 1996.

G. Kresse and D. Joubert. From ultrasoft pseudopotentials to the projector augmented-wave method. <u>Phys. Rev. B</u>, 59:1758–1775, Jan 1999.

²⁷ Michael P. Marder. <u>Condensed matter physics</u>. Wiley, 2nd ed. edition, 2010.

²⁸ Tue Gunst, Troels Markussen, Kurt Stokbro, and Mads Brandbyge. First-principles method for electron-phonon coupling and electron mobility: Applications to twodimensional materials. Phys. Rev. B, 93:035414, Jan 2016.

²⁹ Shouhang Li, Zhen Tong, Xinyu Zhang, and Hua Bao. Thermal conductivity and lorenz ratio of metals at intermediate temperatures with mode-level first-principles analysis. Phys. Rev. B, 102:174306, Nov 2020.

J. M. Ziman. <u>Principles of the Theory of Solids</u>. Cambridge University Press, 2 edition, 1972.

³¹ Ali Lavasani, Daniel Bulmash, and Sankar Das Sarma. Wiedemann-franz law and fermi liquids. <u>Phys. Rev. B</u>, 99:085104, Feb 2019.

³² Thibault Sohier, Davide Campi, Nicola Marzari, and Marco Gibertini. Mobility of two-dimensional materials from first principles in an accurate and automated framework. Phys. Rev. Mater., 2:114010, Nov 2018.

H. Bruns. Zur theorie der kugelfunctionen. <u>Journal für die</u> reine und angewandte Mathematik, 90:322–328, 1881.

Gábor Szegö. Orthogonal Polynomials. American Mathematical Society, Providence, RI, 1975.

35 https://phonopy.github.io/phelel/.

Alexander H. Barnett, Jeremy Magland, and Ludvig af Klinteberg. A parallel nonuniform fast fourier transform library based on an "exponential of semicircle" kernel. <u>SIAM Journal on Scientific Computing</u>, 41(5):C479–C504, 2019.

³⁷ P. Vogl. Microscopic theory of electron-phonon interaction in insulators or semiconductors. <u>Physical Review B</u>, 13(2):694–704, January 1976.

³⁸ Supplemental material.

³⁹ John P. Perdew, Adrienn Ruzsinszky, Gábor I. Csonka, Oleg A. Vydrov, Gustavo E. Scuseria, Lucian A. Constantin, Xiaolan Zhou, and Kieron Burke. Restoring the density-gradient expansion for exchange in solids and surfaces. Phys. Rev. Lett., 100:136406, Apr 2008. John P. Perdew, Kieron Burke, and Matthias Ernzerhof. Generalized gradient approximation made simple. <u>Phys.</u> Rev. Lett., 77:3865–3868, Oct 1996.

⁴¹ Kerstin Hummer, Andreas Grüneis, and Georg Kresse. Structural and electronic properties of lead chalcogenides from first principles. <u>Physical Review B</u>, 75(19):195211, May 2007. Publisher: <u>American Physical Society</u>.

⁴² Atsushi Togo, Laurent Chaput, Terumasa Tadano, and Isao Tanaka. Implementation strategies in phonopy and phono3py. J. Phys. Condens. Matter, 35(35):353001, 2023.

⁴³ Atsushi Togo. First-principles phonon calculations with phonopy and phono3py. J. Phys. Soc. Jpn., 92(1):012001, 2023.

⁴⁴ Atsuto Seko and Atsushi Togo. Projector-based efficient estimation of force constants. <u>Phys. Rev. B</u>, 110:214302, Dec 2024.

⁴⁵ Yoyo Hinuma, Giovanni Pizzi, Yu Kumagai, Fumiyasu Oba, and Isao Tanaka. Band structure diagram paths based on crystallography. <u>Computational Materials</u> Science, 128:140–184, 2017.

Kohei Shinohara Atsushi Togo and Isao Tanaka. Spglib: a software library for crystal symmetry search. Science and Technology of Advanced Materials: Methods, 4(1):2384822, 2024.

⁴⁷ Pedro Borlido, Thorsten Aull, Ahmad Huran, Fabien Tran, Miguel Marques, and Silvana Botti. Large-scale benchmark of exchange-correlation functionals for the determination of electronic band gaps of solids. <u>Journal of</u> Chemical Theory and Computation, 15, 07 2019.

Priyanka Jood, James P. Male, Shashwat Anand, Yoshitaka Matsushita, Yoshiki Takagiwa, Mercouri G. Kanatzidis, G. Jeffrey Snyder, and Michihiro Ohta. Na doping in pbte: Solubility, band convergence, phase boundary mapping, and thermoelectric properties. Journal of the American Chemical Society, 142(36):15464–15475, 2020. PMID: 32786772.

⁴⁹ Qian Zhang, Feng Cao, Weishu Liu, Kevin Lukas, Bo Yu, Shuo Chen, Cyril Opeil, David Broido, Gang Chen, and Zhifeng Ren. Heavy doping and band engineering by potassium to improve the thermoelectric figure of merit in p-type pbte, pbse, and pbte1-ysey. <u>Journal of the American Chemical Society</u>, 134(24):10031-10038, 2012. PMID: 22676702.

Jun ichi Tani and Hiroyasu Kido. Thermoelectric properties of sb-doped mg2si semiconductors. <u>Intermetallics</u>, 15(9):1202–1207, 2007.

⁵¹ H.L. Gao, T.J. Zhu, X.B. Zhao, and Y. Deng. Influence of sb doping on thermoelectric properties of mg2ge materials. Intermetallics, 56:33–36, 2015.

Wataru Saito, Kei Hayashi, Zhicheng Huang, Jinfeng Dong, Jing Feng Li, and Yuzuru Miyazaki. Enhancing the thermoelectric performance of mg2sn single crystals via point defect engineering and sb doping. ACS applied materials and interfaces, 12(52):57888−57897, December 2020. Publisher Copyright: © 2020 American Chemical Society.

Wuyang Ren, Hangtian Zhu, Jun Mao, Li You, Shaowei Song, Tian Tong, Jiming Bao, Jun Luo, Zhiming Wang, and Zhifeng Ren. Manipulation of ni interstitials for realizing large power factor in tinisn-based materials. <u>Advanced Electronic Materials</u>, 5(7):1900166, 2019.

Hanhui Xie, Heng Wang, Chenguang Fu, Yintu Liu, G. Jeffrey Snyder, Xinbing Zhao, and Tiejun Zhu. The intrinsic

disorder related alloy scattering in zrnisn half-heusler thermoelectric materials. Sci Rep, 4:6888, 2014.

⁵⁵ Cui Yu, Tie-Jun Zhu, Rui-Zhi Shi, Yun Zhang, Xin-Bing Zhao, and Jian He. High-performance half-heusler thermoelectric materials hf_{1-x}zr_xnisn_{1-y}sb_y prepared by levitation melting and spark plasma sintering. <u>Acta Materialia</u>, 57(9):2757-2764, 2009.

⁵⁶ L. Jodin, J. Tobola, P. Pecheur, H. Scherrer, and S. Kaprzyk. Effect of substitutions and defects in halfheusler FeVSb studied by electron transport measurements and kkr-cpa electronic structure calculations. <u>Phys. Rev.</u> B, 70:184207, Nov 2004.

⁵⁷ E. Flage-Larsen and Ø. Prytz. The lorenz function: Its properties at optimum thermoelectric figure-of-merit. Applied Physics Letters, 99(20):202108, 11 2011.

Hyun-Sik Kim, Zachary M. Gibbs, Yinglu Tang, Heng Wang, and G. Jeffrey Snyder. Characterization of lorenz number with seebeck coefficient measurement. <u>APL</u> Materials, 3(4):041506, 02 2015.

Xufeng Wang, Vahid Askarpour, Jesse Maassen, and Mark Lundstrom. On the calculation of lorenz numbers for complex thermoelectric materials. <u>Journal of Applied Physics</u>, 123(5):055104, 02 2018.

Mischa Thesberg, Hans Kosina, and Neophytos Neophytou. On the lorenz number of multiband materials. <u>Phys.</u> Rev. B, 95:125206, Mar 2017.

G. Grimvall. The Electron-phonon Interaction in Metals. Science Education and Future Human Needs Series. North-Holland Publishing Company, 1981.

Libin Zhang, Penghao Xiao, Li Shi, Graeme Henkelman, John B. Goodenough, and Jianshi Zhou. Suppressing the bipolar contribution to the thermoelectric properties of mg2si0.4sn0.6 by ge substitution. <u>Journal of Applied Physics</u>, 117(15):155103, 04 2015.

63 Shin-ichiro Tamura. Isotope scattering of dispersive phonons in ge. Phys. Rev. B, 27:858–866, Jan 1983.

Yanzhong Pei, Xiaoya Shi, Aaron LaLonde, Heng Wang, Lidong Chen, and G Jeffrey Snyder. Convergence of electronic bands for high performance bulk thermoelectrics. Nature, 473(7345):66—69, May 2011.

⁶⁵ P. P. Debye and E. M. Conwell. Electrical properties of n-type germanium. Phys. Rev., 93:693–706, Feb 1954.

Samuel Poncé, Elena R. Margine, and Feliciano Giustino. Towards predictive many-body calculations of phonon-limited carrier mobilities in semiconductors. Phys. Rev. B, 97:121201, Mar 2018.

⁶⁷ Nakib H. Protik, Chunhua Li, Miguel Pruneda, David Broido, and Pablo Ordejón. The elphbolt ab initio solver for the coupled electron-phonon boltzmann transport equations. npj Computational Materials, 8(1), February 2022.

⁶⁸ D. Chattopadhyay and H. J. Queisser. Electron scattering by ionized impurities in semiconductors. <u>Rev. Mod. Phys.</u>, 53:745–768, Oct 1981. ⁶⁹ Ransell D'Souza, Jiang Cao, José D. Querales-Flores, Stephen Fahy, and Ivana Savić. Electron-phonon scattering and thermoelectric transport in p-type pbte from first principles. Phys. Rev. B, 102:115204, Sep 2020.

P. Giraldo-Gallo, B. Sangiorgio, P. Walmsley, H. J. Silverstein, M. Fechner, S. C. Riggs, T. H. Geballe, N. A. Spaldin, and I. R. Fisher. Fermi surface evolution of nadoped pbte studied through density functional theory calculations and shubnikov-de haas measurements. Phys. Rev. B, 94:195141, Nov 2016.

⁷¹ K. Parlinski, Z. Q. Li, and Y. Kawazoe. First-principles determination of the soft mode in cubic zro₂. Phys. Rev. Lett., 78:4063–4066, May 1997.

⁷² Yoon-Suk Kim, Martijn Marsman, Georg Kresse, Fabien Tran, and Peter Blaha. Towards efficient band structure and effective mass calculations for III-V direct bandgap semiconductors. Physical Review B, 82(20):205212, November 2010. Publisher: American Physical Society.

⁷³ J. Callaway. <u>Quantum Theory of the Solid State</u>. Academic Press, 1974.

⁷⁴ M. Gajdoš, K. Hummer, G. Kresse, J. Furthmüller, and F. Bechstedt. Linear optical properties in the projectoraugmented wave methodology. <u>Phys. Rev. B</u>, 73:045112, Jan 2006.

⁷⁵ C. Jacoboni, C. Canali, G. Ottaviani, and A. Alberigi Quaranta. A review of some charge transport properties of silicon. Solid-State Electronics, 20(2):77–89, 1977.

⁷⁶ I-Te Lu, Jin-Jian Zhou, Jinsoo Park, and Marco Bernardi. First-principles ionized-impurity scattering and charge transport in doped materials. <u>Phys. Rev. Mater.</u>, 6:L010801, Jan 2022.

O. D. Restrepo, K. Varga, and S. T. Pantelides. First-principles calculations of electron mobilities in silicon: Phonon and coulomb scattering. <u>Applied Physics Letters</u>, 94(21):212103, 05 2009.

⁷⁸ Sheng S. Li and W. Robert Thurber. The dopant density and temperature dependence of electron mobility and resistivity in n-type silicon. <u>Solid-State Electronics</u>, 20(7):609– 616, 1977.

⁷⁹ C. Canali, C. Jacoboni, F. Nava, G. Ottaviani, and A. Alberigi-Quaranta. Electron drift velocity in silicon. Phys. Rev. B, 12:2265–2284, Sep 1975.

⁸⁰ Chikako Yamanouchi, Kanji Mizuguchi, and Wataru Sasaki. Electric conduction in phosphorus doped silicon at low temperatures. <u>Journal of the Physical Society of Japan</u>, 22(3):859–864, 1967.

Nicolas Roisin, Guillaume Brunin, Gian-Marco Rignanese, Denis Flandre, Jean-Pierre Raskin, and Samuel Poncé. Phonon-limited mobility for electrons and holes in highly-strained silicon. npj Computational Materials, 10(1):242, oct 2024

Heng Wang, Yanzhong Pei, Aaron D. LaLonde, and G. Jeffrey Snyder. Heavily doped p-type pbse with high thermoelectric performance: An alternative for pbte. <u>Advanced Materials</u>, 23(11):1366–1370, 2011.